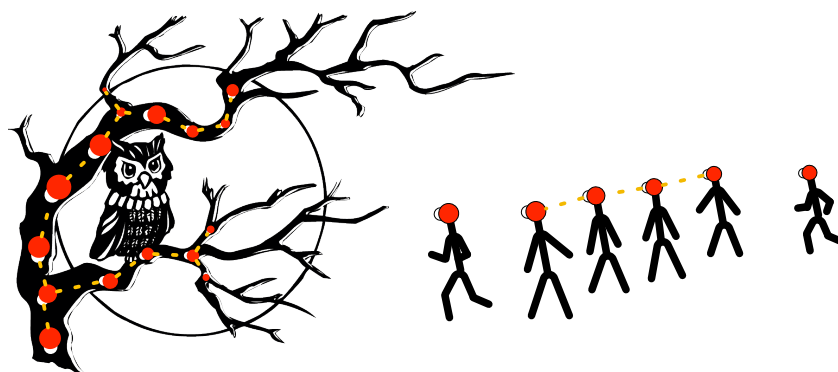


Thesis for the Degree of Doctor of Philosophy

Trees, Queues and Alcohols



Per Sillrén

CHALMERS

Applied Physics
Chalmers University of Technology
November 2013

Trees, Queues and Alcohols
PER SILLRÉN
Göteborg, Sweden 2013
ISBN 978-91-7385-932-5

Doktorsavhandlingar vid Chalmers tekniska högskola
Ny serie Nr 3613
ISSN 0346-718X

©PER SILLRÉN, 2013

Applied Physics
Chalmers University of Technology
SE-412 96 Göteborg, Sweden

Chalmers Reproservice
Göteborg, Sweden 2013

Trees, Queues and Alcohols

Per Sillrén

Department of Applied Physics
Chalmers University of Technology
SE-412 96 Göteborg, Sweden

Abstract

Hydrogen bonded (H-bonded) materials, such as water, alcohols, sugars, and even DNA, are extremely important for biology, as well as chemical industry. Alcohols are used as solvents in paints, in perfumes, as cleaners, anti-freezers, or as an alternative to petrol in combustion engines. Crucial in most of the applications are the effects the hydrogen bonds have on the physical properties of the liquid and its functionality.

This thesis is concerned with the H-bonding structure and dynamics in some of the simplest H-bonding material: small molecule alcohols. To investigate the structure and dynamics of the H-bonded clusters we use a combination of experimental, computational, and theoretical methods. More specifically, a statistical model of the hydrogen bonded clusters is developed that describes the distribution of cluster sizes and their properties. The clusters that we find, have a tree-like topology, and a broad distribution of cluster sizes. The model properties are in good agreement with results from Monte Carlo simulations as well as EPSR simulations based on neutron diffraction data. The model is also shown to be compatible with spectroscopic IR- and Raman data.

The dynamics of the clusters are captured in a model inspired by queuing theory, with monomers leaving and joining the clusters. The dipole correlation spectrum of the dynamic model explains the Debye peak seen in dielectric spectra, and also the different time scales measured by NMR and neutron scattering techniques.

Keywords: Alcohols, Hydrogen Bonded Liquids, Neutron Scattering, Monte Carlo Simulation, EPSR, Raman Scattering, Statistical Physics

Acknowledgments

First of all, I would like to thank everyone who has been involved in the research presented in this thesis; my supervisors Aleksandar Matic and Johan Mattsson, the rest of the co-authors on the papers; Johan Bielecki, Jan Swenson, Daniel Bowron, Sebastian Schildmann, Catalin Gainaru and Roland Böhmer. It's been great working with you all!

A great big thanks also to the members of the KMF group, past and present, and especially to my office mates for the most part of the time, Johan and Susanne. In the lonely world of academic research, nice colleagues are more important than anything else!

A big Thank You also to the fantastic Glass and Time group at Roskilde University, the time spent with you at Sømimestationen, in Gothenburg, Copenhagen, Rome and Barcelona have been truly great from both a scientific and social perspective!

Mom, thanks for always encouraging my natural aptitude for technology and my scientific curiosity. And for coping with me always disassembling everything you ever gave me.

Granddad Ove, you were my technical role model, showing me that nothing is too complicated to try to understand or fix!

Linnea, Alma, and Vide, hopefully you will enjoy a larger portion of my commitment from here on, as I no longer have a thesis to be anxious about. I love you more than anything else!

List of Publications

I. A statistical model of hydrogen bond networks in liquid alcohols

Per Sillrén, Johan Bielecki, Johan Mattsson, Lars Börjesson, and Aleksandar Matic

J. Chem. Phys., **136**, 094514 (2012)

II. Temperature dependence of the hydrogen bond structure of liquid 1-propanol by neutron diffraction and EPSR Simulations

Per Sillrén, Jan Swenson, Johan Mattsson, Daniel Bowron, and Aleksandar Matic

J. Chem. Phys., **138**, 214501 (2013)

III. On the use of vibrational spectroscopy to determine the temperature dependent hydrogen bond structure in alcohols

Per Sillrén, Erlendur Jónsson, Johan Bielecki, Johan Mattsson, and Aleksandar Matic

Manuscript

IV. Queueing theory unravels the transient H-bonded chain dynamics in liquid alcohols

Per Sillrén and Aleksandar Matic

Submitted

V. High-frequency properties of liquid 1-propanol studied by neutron scattering, near-infrared, and dielectric spectroscopy

Per Sillrén, Aleksandar Matic, Maths Karlsson, Michael Marek Koza, Marco Maccarini, Peter Fouquet, Marion Götz, Thomas Bauer, Rudolf Gulich, Peter Lunkenheimer, Alois Loidl, Johan Mattsson, Catalin Gainaru, Eugen Vynokur, Sebastian Schildmann, Stefan Bauer, Roland Böhmer

Submitted to J. Chem. Phys.

My contributions to the papers

Paper I

I formulated the model and derived the recursive cluster size distribution and its properties except the higher order moments. I performed to MC simulations and developed a program running alongside the simulation, that calculated the cluster properties presented in the paper. I was the main author of the manuscript.

Paper II

I performed the raw data treatment in GudrunN, performed the EPSR simulations and subsequent analysis and was the main author of the manuscript.

Paper III

I prepared samples, performed the measurements, developed the analysis method combining our model from Paper I with DFT calculations and was the main author of the manuscript.

Paper IV

I developed the theory, performed the calculations and simulations and was the main author of the manuscript.

Paper V

I prepared samples and, together with some of the co-authors, performed the neutron scattering experiments. I analysed the neutron scattering data, and wrote the initial version of the manuscript focusing on the NSE and QENS results.

Contents

1	Introduction	1
2	The Liquid State	5
2.1	From Potential Energy to Structure and Thermodynamics	6
2.2	Dynamics, autocorrelation functions and response functions	8
3	The Structure and Dynamics of Hydrogen Bonded Liquids	11
3.1	Structure of the Hydrogen Bond Network in Alcohols	11
3.2	Dynamics in alcohols	14
4	Statistical Models of Hydrogen Bonded Clusters in Alcohols	17
4.1	A model describing the tree-like structure of the H-bonded alcohol clusters	19
4.1.1	Cluster size distribution	20
4.1.2	Moments of the cluster size distribution	21
4.2	A quantitative model for the transient chain dynamics in alcohols	23
4.2.1	The dipole moment distribution	26
4.2.2	The dipole moment autocorrelation function	26
5	Neutron Scattering	29
5.1	Probing the Structure using neutron diffraction	29
5.2	Probing dynamics using QENS and NSE	34
5.2.1	Quasi elastic neutron scattering	35
5.2.2	Neutron spin echo	36
6	Raman Spectroscopy	39
6.1	Classical Theory of Raman Scattering	39
6.2	A Few Words About Units	41
6.3	Quantum Theory of Raman Scattering	42
6.3.1	Derivation of the General Polarisability Tensor	42
6.3.2	Simplification of the Polarisability Tensor	44
6.3.3	The Harmonic Oscillator Approximation	45
6.3.4	Scattering From a Collection of Molecules	46

6.4	The Role of Symmetries in Raman Scattering	46
6.4.1	Molecular symmetries	47
6.4.2	Symmetry selection rule	49
6.5	Line Shapes in Vibrational Spectra	50
6.5.1	Kubo's model	51
6.5.2	A Generalised Kubo Model	53
6.6	The Dilor Spectrometer	54
7	Monte Carlo and EPSR Simulations	55
7.1	The Metropolis Algorithm	55
7.2	Intermolecular Interactions - OPLS-AA	57
7.3	Intramolecular interactions	57
7.4	The EPSR technique	58
8	Summary of Appended Papers	59
	Bibliography	64

1

Introduction

Hydrogen bonded (H-bonded) materials are all around us. The most abundant one, water, covers 71% of the earth's surface, and constitutes about 60% of our bodies. Water has some unusual properties, caused by the H-bonds, including a density maximum at 4° C and a compressibility minimum at 46° C [1]. Not only does the water in our bodies contain H-bonds, but also sugars, fatty acids and proteins interact via H-bonds [2, 3]. In medicine, the polymeric alcohol polyethylene glycol, PEG, is used in a process called pegylation [4], where PEG chains are attached to drugs or therapeutic proteins. Pegylation can prolong the medicines half life in the body, as well as aid in making the drug water soluble. Anomalies caused by hydrogen bonds are also found in water-alcohol mixtures [5], as well as in pure alcohols [6]. In mono alcohols, the most well known anomaly is probably the so called Debye process seen in dielectric spectra [1, 5–8].

To better understand the effect H-bonds have in different materials, it is important to know what the H-bonded structures look like, and what the connection is between these structures and their dynamics. H-bonds are intermolecular bonds, with a bond strength corresponding to ~ 10 times the kinetic energy of the hydrogen bonding atoms at room temperature. In alcohols and water, this leads to a transient H-bond network [9], where molecules leave and join the networks at picosecond timescales.

There is thus a great need to systematically study how H-bonding affects a materials properties. One might think that water, being the smallest and structurally simplest H-bonding molecule, would be the ideal candidate for studying the effect of H-bonding in general. The H-bonding situation in water is complicated, however, by the fact that a single water molecule can participate in as many as four H-bonds. Alcohols, especially mono-alcohols, are also relatively simple molecules, but have the advantage that one can vary the properties of the molecule, such as the length of the alkyl tail, or the position of the OH-group

in a systematic way. One can then study how the H-bonded structures in the liquid changes, and relate that to variations in other properties. Mono-alcohols are thus a class of materials well suited for systematic exploration of the effects of H-bonding. Both water and alcohols have, as discussed in more detail in chapter 3, been studied extensively over the last century, but details regarding the structure of the H-bonded molecule clusters in these liquid still remain unclear. The main questions regarding the structure of H-bonded liquids that I investigate in my thesis are

- What is the topology of the hydrogen bonded clusters formed in liquid alcohols?
- How can we describe and quantify these structures?
- How do we access the structural properties experimentally?
- What happens to the structure when we change the temperature of the liquids?

To answer these questions I have developed a statistical model for the hydrogen bonded clusters, based on the probabilities of forming bonds between neighbouring molecules. The model, presented in Paper I and in chapter 4 is shown to be capable of describing the, tree-like, hydrogen bonded clusters obtained from Monte Carlo computer simulations of a variety of mono and poly alcohols. In Paper II and Paper V the model is shown to also be in good agreement with results based on neutron diffraction data and Raman spectroscopy.

Hydrogen bonds have a strength intermediate between other typical intermolecular bonds, and intramolecular bonds [10]. The strength is such that the bonds break and reform on a picosecond timescale at room temperature, leading to rapidly evolving sizes and shapes of the intermolecular clusters mentioned above. In Paper IV we develop a mathematical model, based on results from queueing theory, which is shown to be consistent with one of the unusual features of monohydroxy alcohols: the so called Debye peak seen in dielectric spectra. The dynamic model also explains a different time scale that shows up in NMR measurements [9] and in the neutron scattering experiments of Paper V. Both timescales are shown to be connected to the size distribution of the hydrogen bonded clusters present in mono alcohols.

Figure 1.1 display the molecular structure of the alcohols studied in the appended papers and table 1.1 lists some of their basic thermodynamic properties.

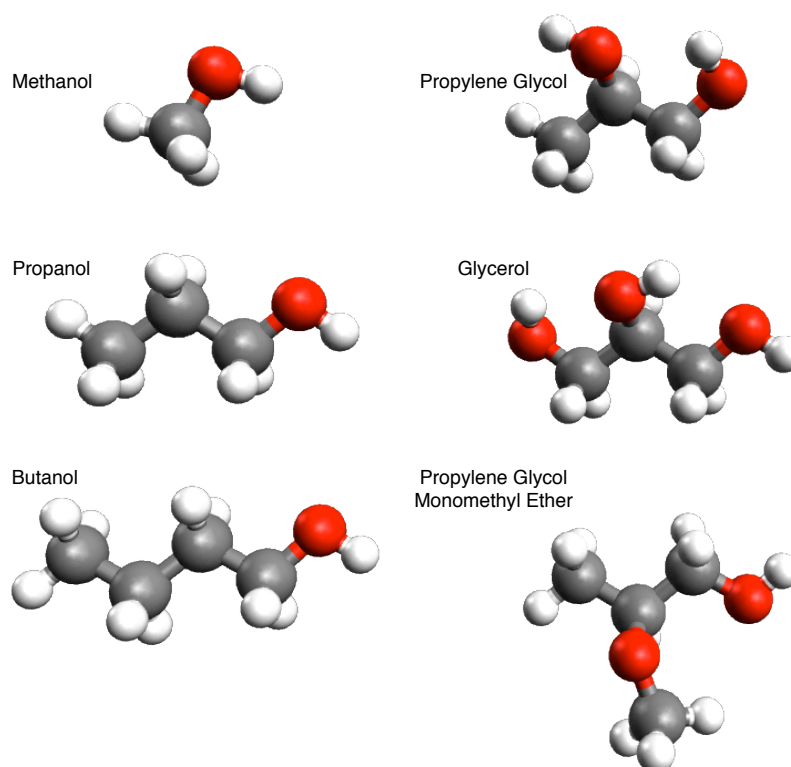


Figure 1.1: The six different alcohols studied in the appended papers

Alcohol	Density	Melting temperature	Boiling temperature
Methanol	0.79 g/cm ³	-97° C	65° C
Propanol	0.80 g/cm ³	-126° C	97° C
Butanol	0.81 g/cm ³	-90° C	118° C
Propylene glycol	1.04 g/cm ³	-59° C	188° C
Glycerol	1.26 g/cm ³	18° C	290° C
Propylene glycol monomethyl ether	0.96 g/cm ³	-97° C	118° C

Table 1.1: Densities, melting points, and boiling points of the six alcohols studied in the appended papers

2

The Liquid State

From an energetic point of view, liquids are characterised by a total potential energy V_N that is of the same order of magnitude as their total kinetic energy K_N [11]

$$\frac{K_N}{|V_N|} \sim 1, \quad (2.1)$$

where N is the number of atoms in the liquid. The kinetic energy is related to the temperature through the equipartition theorem

$$K_N = N \frac{3}{2} k_B T, \quad (2.2)$$

where k_B is Boltzmann's constant and T is the temperature of the liquid. The right hand side, $k_B T$ is called the thermal energy of the system, and it follows that in a liquid, the thermal energy is also of the same order of magnitude as the average potential energy

$$k_B T \sim \frac{2|V_N|}{3N}, \quad (2.3)$$

which makes it possible for the molecules to move far enough away from their attracting neighbours to make the liquid deformable, but not far enough to break up the liquid into a gas.

The total potential energy can be divided into different contributions with different strengths and different directional properties. At close distances, the dominant part, present in all liquids, is the hard core repulsion connected to the Pauli exclusion principle, which forbids the overlap of electron clouds of neighbouring molecules. Also present in all liquids, are the attractive *van der Waals interactions* [10], caused by permanent or induced multipole-multipole interactions, i.e. from the interaction between the charge distributions of the molecules. In non-polar liquids, the dominant van der Waals interaction is that between two

induced dipole moments, also called London interaction or dispersion interaction. In polar liquids on the other hand, the permanent dipoles dominate the attractive part of the interaction, and in liquids such as water and alcohols containing one or more hydrogen atom covalently bonded to an oxygen, an OH-group, these interactions give the largest contribution to the so called hydrogen bonds (OH-bonds) that this thesis is to a very large extent about.

2.1 From Potential Energy to Structure and Thermodynamics

The potential energy, V_N , is related to the structure of a liquid, through the radial distribution function, $g(r)$, which for a monatomic, homogeneous, and isotropic liquid is defined as [11]

$$\begin{aligned}\rho g(r) &= \rho^{(2)}(r) = \left\langle \frac{1}{N} \sum_{i=1}^N \sum_{j \neq i}^N \delta(\mathbf{r} - \mathbf{r}_j + \mathbf{r}_i) \right\rangle \\ &= \frac{N-1}{Z_N} \int \int \dots \int e^{-\frac{V_N(\mathbf{r}+\mathbf{r}_2, \mathbf{r}_2, \mathbf{r}_3, \dots, \mathbf{r}_N)}{k_B T}} d\mathbf{r}_2 d\mathbf{r}_3 \dots d\mathbf{r}_N, \quad (2.4)\end{aligned}$$

where r is the distance between two atoms, $\rho = N/V$ is the number density of the liquid (N is the number of molecules, V is the volume of the liquid), and Z_N is the configuration integral.

The connection to potential energy is through the Boltzmann factor $e^{-\frac{V_N}{k_B T}}$, and the connection to structure is the fact that the probability of finding one particle at a distance r from a reference particle is $4\pi r^2 \rho g(r) dr$, and peaks in $g(r)$ represent shells of neighbouring particles around the reference particle. The number of nearest neighbours a given particle has is thus the integral of $4\pi r^2 \rho g(r)$ over the first peak in $g(r)$. For a polyatomic or molecular system, we can define, analogous to equation (2.4), partial pair correlations between different atom types. This will be elaborated upon further in chapter 5, where it will also be explained how the pair correlations can be measured by neutron diffraction experiments.

An example of a partial radial distribution function for 1-propanol is shown in figure 2.1. The typical intermolecular H-bonded O \cdots H distance is seen to be $\sim 1.8 \text{ \AA}$, and the next nearest neighbour represented by the second peak is seen to be located about 3.4 \AA away. Beyond $r > 4 \text{ \AA}$, there is very little structure left.

If the potential energy is expressed as a sum of pairwise interactions between atoms, i and j ,

$$V_N = \sum_{i=1}^N \sum_{j>i}^N v(r_{ij}), \quad (2.5)$$

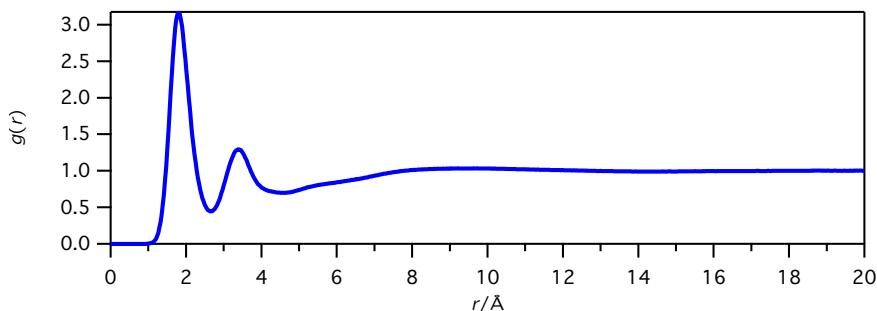


Figure 2.1: The intermolecular (excluding intramolecular correlations) partial radial distribution function, $g_{\text{OH}}(r)$, from EPSR simulations, reflecting the distribution of oxygen around hydroxyl-hydrogens, or vice versa, in liquid 1-propanol at room temperature. The short range order, with one or two clear peaks in the radial distribution functions, is very characteristic of the liquid state.

which is often a good approximation, the pair distribution can also be related to various thermodynamic quantities. One example is the relation between pressure and intermolecular forces, referred to as the virial equation [11]

$$P = k_B T \rho - \frac{2\pi\rho^2}{3} \int r \frac{dv}{dr} g(r) r^2 dr \quad (2.6)$$

When it comes to H-bonds however, the pairwise interaction terms only account for about 70% of the energy [12], and higher order interactions need to be included to yield an accurate description.

The partial pair distribution functions between the different atomic species of a material can in principle be determined experimentally through neutron- or X-ray scattering experiments, but in practice this is intractable for all but the simplest molecules. To make the determination more tractable and unambiguous we thus need other means to narrow down the range of possible structures, such as the use of *a priori* information about the internal structure of the molecules, as determined from other techniques. If we are then able to determine the structure experimentally we can of course reverse the reasoning above, and learn about the intermolecular interactions, such as the hydrogen bonds in alcohols and water. This is the essence of the empirical potential structure refinement (EPSR) simulation technique [13], described in detail in chapter 7, which uses the measured structure to alter the intermolecular pair potentials in an iterative manner, such that the agreement between measured and simulated structure improves over the course of the simulation. When a satisfactory agreement has been obtained one can start extracting properties of interest from the simulation. In Paper II we use the EPSR technique together with neutron diffraction data to extract information about the H-bond network in propanol [14].

2.2 Dynamics, autocorrelation functions and response functions

If the time dependence of particle coordinates are taken into account into the pair distribution function we obtain the van Hove correlation function containing information about correlation in time as well as space. $G(\mathbf{r}, t)$ is defined similarly to the radial distribution function (2.4):

$$G(\mathbf{r}, t) = \left\langle \frac{1}{N} \sum_{i=1}^N \sum_{j=1}^N \delta(\mathbf{r} - \mathbf{r}_j(t) + \mathbf{r}_i(0)) \right\rangle. \quad (2.7)$$

The van Hove function will tend to be peaked around values of \mathbf{r} corresponding to units moving together in the liquid, such as neighbouring molecules, or clusters of molecules. For all values of \mathbf{r} , it will decay with respect to time as the molecules move in a diffusive manner, but the rate of decay will vary depending on the nature of the diffusing structures. In chapter 5 it will be explained how the van Hove function can be measured experimentally using quasi elastic neutron scattering or neutron spin echo.

The van Hove function can also be written as an autocorrelation function of the microscopic particle density $\rho(\mathbf{r}, t)$ [11]

$$\begin{aligned} G(\mathbf{r}, t) &= \left\langle \frac{1}{N} \sum_{i=1}^N \sum_{j=1}^N \delta(\mathbf{r} - \mathbf{r}_j(t) + \mathbf{r}_i(0)) \right\rangle \\ &= \left\langle \frac{1}{N} \int \sum_{i=1}^N \sum_{j=1}^N \delta(\mathbf{r} - \mathbf{r}_j(t) + \mathbf{r}') \delta(\mathbf{r}' - \mathbf{r}_i(0)) d\mathbf{r}' \right\rangle \\ &= \left\langle \frac{1}{N} \int \rho(\mathbf{r}' + \mathbf{r}, t) \rho(\mathbf{r}', 0) d\mathbf{r}' \right\rangle \\ &= \frac{1}{\rho} \langle \rho(\mathbf{r}, t) \rho(\mathbf{0}, 0) \rangle. \end{aligned} \quad (2.8)$$

where the microscopic particle density is defined as

$$\rho(\mathbf{r}, t) = \sum_{i=1}^N \delta(\mathbf{r} - \mathbf{r}_i(t)). \quad (2.9)$$

This can be generalised to a general dynamic variable $A(\mathbf{r}, t)$ by writing

$$A(\mathbf{r}, t) = \sum_{i=1}^N a_i(t) \delta(\mathbf{r} - \mathbf{r}_i(t)). \quad (2.10)$$

which has a corresponding autocorrelation function

$$C(\mathbf{r}, t) = \langle A(\mathbf{r}, t)A^*(\mathbf{0}, 0) \rangle, \quad (2.11)$$

where * denotes complex conjugation. A can be charge current, dipole moment, particle velocity or any other property of interest. Now, the fluctuation dissipation theorem states [11] that the imaginary part of the response in the property A with respect to an external field \mathcal{F} , conjugate to the property A , is proportional to the time derivative of the autocorrelation function! Since measurements are more often performed in the frequency domain (and when applicable, wave vector domain), the fluctuation dissipation theorem is often expressed in terms of the space-time Fourier transform of the autocorrelation function, $\hat{C}(Q, \omega)$, as

$$\chi''(Q, \omega) = \frac{\pi\omega}{Vk_B T} \hat{C}(Q, \omega). \quad (2.12)$$

The particular example that will be of interest is when \mathcal{F} is an oscillating external electromagnetic field and A is electrical dipole moments. The experimental technique is then referred to as dielectric spectroscopy, and as will be discussed later in this chapter, mono alcohols have an unusual peak in their dielectric relaxation spectrum (i.e. an unusual dipole-dipole autocorrelation function). The relationship between this unusual relaxation and the H-bonded clusters in alcohols is further explored in chapter 4 and in Paper IV.

3

The Structure and Dynamics of Hydrogen Bonded Liquids

3.1 Structure of the Hydrogen Bond Network in Alcohols

The structure of H-bonded liquids, such as alcohols, can be described in terms of the H-bonded clusters present in the liquids. As can be seen in figure 3.1, showing four example clusters, each OH-group can bond to up to three neighbouring OH-groups. The possible H-bonded structures thus range from chains and loops, to branched tree like structures. The typical H-bonded O—H distance is 1.4 - 2.4 Å. Computational studies have revealed that the H-bonding energy, as well as the OH-stretch vibrational frequency is proportional to the OH-distance [12, 15]. As will be explained below, this sensitivity of the OH-stretch frequency to the H-bonding situation can be used to study the structure of the hydrogen bonded

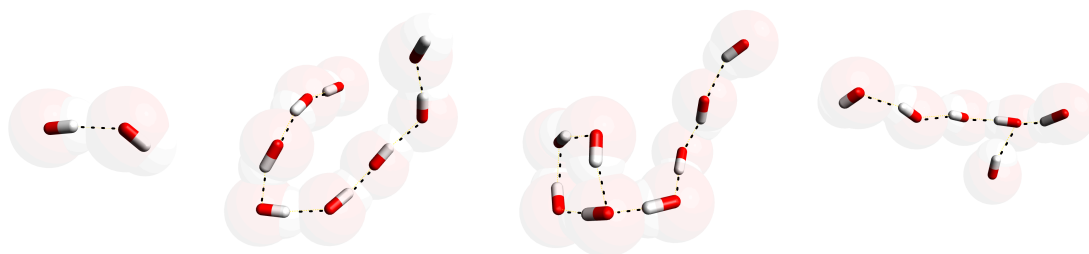


Figure 3.1: Examples of H-bonded clusters from EPSR-simulations of liquid 1-Propanol. Hydrocarbon tails are omitted for clarity.

clusters by spectroscopic techniques. The location of the oxygen electron lone pairs lead to typical H-O—H angles between $100^\circ - 150^\circ$ [14, 16, 17], resulting in curved H-bonded clusters rather than straight chains. To investigate these structures, computational as well as a variety of experimental techniques have been used [9, 14, 16–42].

Since the energy of H-bonds is only about an order of magnitude larger the thermal energy $k_B T$, the energy differences between different types of clusters are small compared to thermal energies, and from the Boltzmann distribution we thus expect a wide range of cluster configurations in a liquid. Thus, even though *ab initio* calculations reveal that ring clusters with 3-5 molecules [15, 34, 38] have the lowest energy, they do not necessarily have to be the dominant cluster type in the liquid. This is especially true since, in *ab initio* calculations, structures of clusters are obtained from a quantum mechanical energy minimisation, and due to the complexity of the quantum mechanical description, these studies are restricted to looking at a small selection of H-bonded clusters, one at a time, rather than at the bulk liquid. Inter-cluster interactions are thus completely ignored.

In contrast to *ab initio* methods, classical molecular dynamics or Monte Carlo simulations can be used to simulate hundreds or even thousands of molecules. When it comes to mono alcohols, the resulting hydrogen bonded clusters are in this case more often found to be in branched chain-like configurations, rather than ring clusters [18, 25, 29–31]. Also experimental data from X-ray or neutron diffraction have suggested that the H-bonded clusters are most often in the form of chains [14, 16, 17, 22, 25, 36, 37] but sometimes also a significant fraction of ring clusters [40, 43] have been claimed to fit with the data. In Paper II we use neutron diffraction data in combination with a type of classical simulation, Empirical Potential Structure Refinement, to study the structure of propanol over a large temperature range.

As mentioned earlier, the frequency of the OH-stretch vibration depends on the hydrogen bonding configuration the OH-group is in. Vibrational spectroscopy such as Raman and IR are therefore viable ways to study the structure of the H-bond network in alcohols and other H-bonded materials. In the gas phase the OH-stretch band is narrow and centred somewhere around $3600 - 3700 \text{ cm}^{-1}$ while in the liquid phase the band is broadened and shifted to frequencies between $3100 \text{ cm}^{-1} - 3700 \text{ cm}^{-1}$, see figure 3.2. The idea is thus to infer the structure from the distribution of OH-frequencies in the liquid. To this end a model introduced by Graener *et al.* [27, 28] with three hydrogen bonding states labeled α/β , γ and δ , has been used [19–21]. α represents non-hydrogen bonded molecules. The alcohol molecules are assumed to form chains with the β molecules representing chain-ends that accept a hydrogen bond and thus have an non-bonded hydrogen atom. γ represents the other kind of chain-end, i.e. molecules that donate a hydrogen bond but has a free non-hydrogen bonded oxygen atom. Finally, δ represents molecules inside the chains that are both donors and acceptors. The

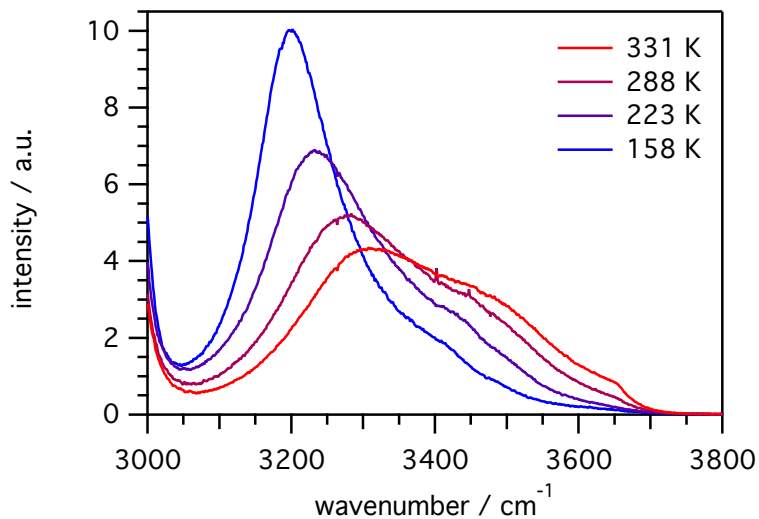


Figure 3.2: The wide OH-stretch Raman spectrum of methanol. As temperature is increased, the spectra shifts towards higher frequencies.

α and β sub-bands are both located close to 3640 cm^{-1} and are therefore treated as one state. The γ sub-band is located around 3490 cm^{-1} and the δ sub-band is located around 3250 cm^{-1} . The relative areas of the bands is then used to obtain fractions of α/β , γ , and δ oscillators that can then be used to obtain the chain length distribution [19–21]. Recent computational work, however, shows that not only the nearest neighbours influence the OH-stretch frequency, but also the next nearest neighbour [15]. Instead of the three OH-stretch sub-bands of Graener *et al.*, it thus seems more appropriate to assign six sub-bands representing different OH-group coordination. *Ab initio* calculations [15, 34] can also be used to calculate the difference in Raman cross-section or IR absorbance between different H-bond configurations. The difference can be more than an order of magnitude, and should thus not be neglected when analysing vibrational spectra. In Paper III we attempt to improve the analysis, for the case of methanol, by taking into account the possibility of branching as well as more detailed information about the vibrational frequencies and cross sections of different hydrogen bonded configurations. In combination with our model from Paper I we obtain cluster size distributions in good agreement with the neutron diffraction results of Paper II.

Also water has been extensively studied using the methods discussed above [44–51]. Even though water might be considered a simpler molecule than alcohols, the H-bonding situation is complicated by the fact that water has four H-bonding sites per molecule, versus the three sites on an alcohol molecule's OH-group.

To conclude, computational as well as diffraction and spectroscopic methods

all provide useful information regarding the structure of H-bond networks in alcohols and other H-bonded materials. None of the mentioned methods are conclusive however, and ideally a combination should be used, and hopefully lead to similar conclusions. Despite all the work that has been done on alcohols there is still no agreement about the types and sizes of H-bonded clusters in these liquids. One problem, in my opinion, has been the lack of quantitative models describing the clusters. This has made it difficult to compare the results of different authors and between different techniques. In Paper I, we thus develop a quantitative model for H-bonded clusters. In Paper I and Paper II the model is compared to results from Monte-Carlo computer simulations and neutron diffraction data. In Paper III we use the model in combination with *ab initio* calculations to extract model parameters and cluster sizes from Raman and IR spectra.

3.2 Dynamics in alcohols

The covalently bonded OH-groups in alcohol molecules vibrate with a frequency of approximately 10^{14} Hz. For each vibrational cycle the probability to escape through the H-bond energy barrier of height $\Delta E_H \approx 10 - 30$ kJ/mol = $4 - 12$ $k_B T$ at room temperature in methanol [15], is given by the Boltzmann factor $e^{-\Delta E_H/k_B T}$. The escape probability per second becomes about 10^{12} giving an H-bond lifetime of 10^{-12} s, in good agreement with experimental findings [52]. The H-bonded clusters are thus constantly reforming, leading to peculiar dynamics that have been studied by a range of techniques, including dielectric spectroscopy [6, 53–67], NMR [9, 68], rheology [54, 69], and by quasi elastic neutron scattering/neutron spin echo in Paper V.

The perhaps most fundamental relaxation process, seen in all above mentioned techniques, is called the structural α relaxation time. The α relaxation time can be approximately related to the mechanical properties of the liquid through the temperature dependent viscosity η and high frequency shear modulus G_∞ [70]

$$\tau_\alpha \approx \frac{\eta}{G_\infty}. \quad (3.1)$$

The α time scale measured by different techniques do usually not match exactly and can vary by as much as an order of magnitude, but generally show very similar temperature dependence [69, 71].

Apart from the ubiquitous α -process, mono alcohols have an unusual relaxation that dominates their dielectric spectrum, as shown in figure 3.3. The peak, referred to as the Debye peak since Debye was the first to study the dielectric properties of alcohols in the early 19th century [72, 73], is about 1-2 decades slower than the α process. The Debye process is characterised by an exponential relaxation, in contrast with the stretched exponential relaxation characterising the α process that is normally the lowest frequency peak in dielectric spectra.

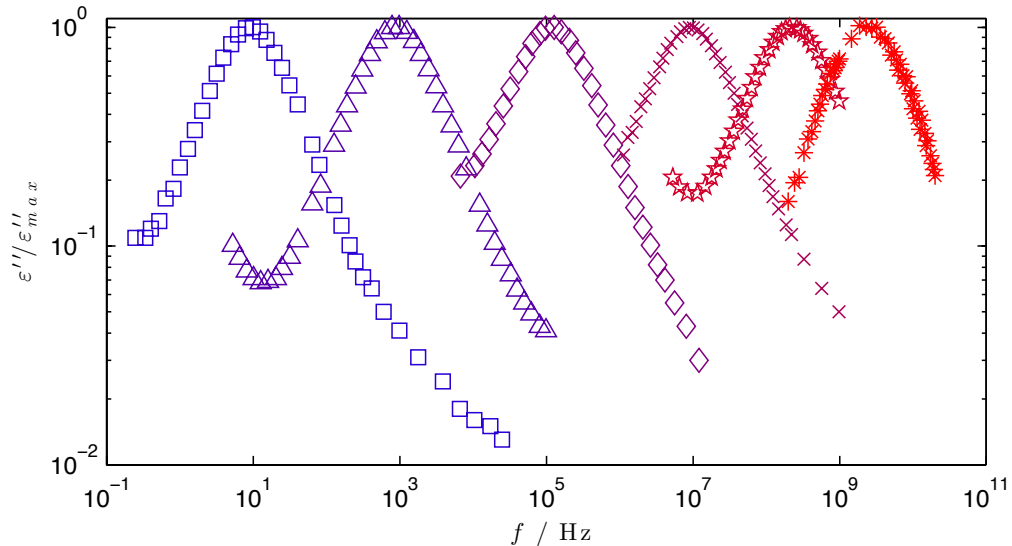


Figure 3.3: Dielectric spectra of 1-propanol, taken from reference [63], showing the large Debye peak dominating the dielectric response. The temperatures, from left to right are 121, 135, 162, 210, 273, and 348 K

The Debye process has been explained in terms of monomers joining and leaving H-bonded clusters, leading to a relaxation of the clusters' dipole moments [9]. Other authors interpret the process as arising from the collisions of monomers as well as the reorientation of H-bonded molecules [74]. It has been shown [6] that the process is largely unaffected, even if the H-bonded clusters are spatially confined to essentially one dimensional tubes, showing that the relaxation does not have to be caused by a spatial reorientation, but could instead be caused by a change in magnitude of the dipole moment as the clusters reform.

A third correlation time, τ_{OH} , has recently been noticed using NMR [9]. This additional relaxation time lies between the α and Debye relaxations, and shows up also in Paper V using neutron scattering.

In Paper IV we extend a simplified version (neglecting branched clusters) of the statistical model presented in Paper I, to also include the transient dynamics of the clusters. According to the dynamic model, the α -relaxation is the time scale of monomers leaving and joining the hydrogen bonded clusters. The average cluster size, $\langle n \rangle$, is shown to be related to τ_α and τ_{OH} through $\tau_{OH} = \langle n \rangle \tau_\alpha$. The Debye relaxation is also connected to the other time scales, and is shown to be the relaxation of the end-to-end dipole moment vector of the whole cluster.

4

Statistical Models of Hydrogen Bonded Clusters in Alcohols

As already mentioned in previous chapters, mono alcohols seem to form tree-like clusters with relatively few branches. In order to relate the properties of such clusters to experimental results, a quantitative description is needed. Models for associating fluids have a history dating back to the early 20th century, when Dolezalek [75] explained the non-ideal properties of mixtures by postulating that one has to take into account not only the properties of the nominal components A and B , but also the associated species A_m , B_n , and A_iB_j ($m, n, i, j \in \mathbb{N}$). Dolezalek's approach belongs to the class of "chemical" theories [76, 77], wherein the distinct cluster types and sizes must be specified in advance, and each cluster type has an associated equilibrium constant acting as a adjustable parameter.

A different class of theories are those based on statistical mechanics. The principle is to start from an intermolecular potential energy, and from that calculate the structure and thermodynamic properties of the liquid. By splitting the potential energy into a reference part, typically something simple, such as a hard sphere repulsion, and a perturbation describing the less trivial interaction, one can express the properties of the associating fluid in terms of the properties of the simple reference fluid. The breakthrough of this type of theories, applied to associated liquids, came with the publication of four papers by Wertheim [78–81] in the 1980's. In his treatment, molecules with association, or bonding, sites, are treated as different species depending on how many bonds are currently active. Based on Wertheim's work, Chapman *et al.* [82, 83], formulated the Statistical Associating Fluid Theory (SAFT) which has received an ever increasing interest since it was introduced [77, 84, 85].

Within the SAFT framework, the free energy of an alcohol is expressed as [82]

$$f = \frac{F}{Nk_B T} = f^{\text{id}} + f^{\text{seg}} + f^{\text{chain}} + f^{\text{assoc}}, \quad (4.1)$$

The first term is an ideal gas contribution, and the second term is the energy contribution from the individual segments of the alcohol, i.e. the CH_n and OH groups hard core and van der Waals type interaction with neighbouring molecules. The third term relates to the covalent bonds between the atoms, and the last term relates to the H-bonding between molecules. f^{assoc} , the most interesting contribution, from the perspective of this thesis, can be related to the fraction ρ_T , of molecules with non-bonded association sites of type T through

$$f^{\text{assoc}} = \sum_T \left(\ln \rho_T - \frac{\rho_T}{2} + \frac{1}{2} \right). \quad (4.2)$$

For the particular case of mono alcohols, two models have been used [86]: 2B and 3B. Both have one bonding site related to the H, and one (2B) or two (3B) bonding sites representing the electron lone pairs on the oxygen. In the SAFT literature [77,82–86], the fraction ρ_T are calculated from the microscopic interaction strengths between the association site, and the potential energy parameters are tuned to match thermodynamic properties, such as density and vapour pressure.

The model presented in Paper I, and summarised in this chapter, is different from the 3B model, in that it treats the two bonding sites on the oxygen as dependent, i.e. the probability that a bond is formed to one of the bonding sites depends on whether a bond already exists on the the other site. The reasoning behind the assumption of dependent bonding probabilities is that, once the first bond is formed, it is difficult for a second molecule's OH group to get in close enough to form a second bond. A second difference is that the parameters of the model are the two bonding probabilities, rather than the potential energy related to the bonding sites. With the SAFT approach, a specific intermolecular association potential fully determines the bonding probabilities, but the opposite relation is of course not true: A given set of probabilities can correspond to several potential energy functions. Our model thus focuses on the structural properties of the H-bonded clusters, without specifying any details of the underlying H-bonding interaction.

Similar models, based on bonding probabilities are common also in polymer science, where they are used to describe polymers with different degree of branching [87,88]. Those models however, are just like the SAFT models mentioned above, based on *distinct* bonding sites, while our model has two *identical* bonding sites, but with probabilities that depend on whether the other site is bonded or not.

In principle, we could take our model and plug in the fractions ρ_T into SAFT framework (equation 4.2), but instead we have focused on comparing the properties of the model's clusters to results from simulations and experimental results:

In Paper I, the validity of our model is compared with clusters obtained from Monte Carlo computer simulation results. In Paper II the model is compared to neutron diffraction results, and in Paper III it is related to vibrational IR and Raman spectra in the OH-stretch region. The model is also summarised here, with some results derived in a more elegant way compared to Paper I.

The last part of the chapter is devoted to our mathematical description of the transient chain model, also presented more briefly in Paper IV, As mentioned in the previous chapter, a distinguishing feature of the H-bonds in alcohols is their short lifetimes, typically only a few pico seconds at room temperature. The transient chain theory, which we formulate in mathematical terms, was originally proposed, by Böhmer and co-workers, based on results from NMR measurements [9]. By also measuring the self diffusion constant and comparing to viscosity data, they concluded that the previously mentioned Debye process seen in alcohols cannot be related to the diffusion of whole H-bonded clusters, but must instead be the signature of a process where monomers leave and join the clusters in a queue-like fashion, i.e. one by one, at the ends. To make the calculations feasible, the mathematical transient chain model presented here is based on the assumption of zero branching probability, resulting in chain-like, rather than the tree-like structures of our structure model. This approximation is justified by results connected to the tree model however, where the branching probability is typically rather small, $< 10\%$ [14, 18].

4.1 A model describing the tree-like structure of the H-bonded alcohol clusters

The tree model is constructed by starting with an OH-group and assigning a probability $p(O_A) = p_A$ of forming a first hydrogen bond, designated O_A , from the oxygen to a neighbouring group, and a probability $p(O_B|O_A) = p_B$ of forming a second hH-bond O_B to a second neighbour, given that the first bond, O_A , is already in place. We will also need to know the unconditional probability $p(O_B)$ which is easily calculated using Bayes' theorem:

$$p(O_B) = \frac{p(O_B|O_A)p(O_A)}{p(O_A|O_B)} = \frac{p_B p_A}{1} = p_A p_B. \quad (4.3)$$

An example of a tree, with three leaves, generated in this fashion is shown in figure 4.1.

The tree structures described by our model, referred to as “unary/binary trees” or “Motzkin trees”, have been previously discussed in terms of combinatoric properties [89], but we have not found any references to *random* unary/binary trees in the literature.

For clusters of size three we have two possibilities: a linear cluster or a branched one. The linear one has probability $p_A(1 - p_B)r(2)$, while the branched one has probability $p_A p_B (r(1))^2$ giving

$$r(3) = p_1 r(2) + p_2 (r(1))^2. \quad (4.8)$$

A tree with four OH-groups can be constructed in three different ways; start from one OH-group and add a cluster of size 3, start from one OH-group and add a cluster of size 1 to the first branch and a cluster of size 2 to the second branch or vice versa. In total we thus get

$$r(4) = p_1 r(3) + p_2 r(1)r(2) + p_2 r(2)r(1). \quad (4.9)$$

By continuing in this way, we get for a general n

$$r(n) = \delta_{n,1} p_0 + p_1 r(n-1) + p_2 \sum_{k=1}^{\infty} r(k)r(n-k-1), \quad (4.10)$$

where the extension of the sum to infinity is valid as long as $r(n) = 0$ for $n < 1$.

The cluster size distribution can also be expressed in closed form, by noting that

$$a_{n,k} = \frac{1}{n} \binom{n}{k+1} \binom{n-k-1}{k}, \quad (4.11)$$

denotes the number of trees with n nodes, $k+1$ leaves, and k branch points. The probability of getting one specific tree of this kind is $p_1^{n-2k-1} p_2^k p_0^{k+1}$ and the probability of getting *any* tree of this kind can thus be written

$$r(n, k) = a_{n,k} p_1^{n-2k-1} p_2^k p_0^{k+1}. \quad (4.12)$$

The cluster size distribution is then obtained by summing over the different possible number of branches for a given tree size

$$r(n) = \sum_{k=0}^{\infty} r(n, k), \quad (4.13)$$

where we have extended the sum to infinity, since $a_{n,k}$ is zero for $k > n/2 - 1$, which is the maximum number of branches on a tree of size n .

4.1.2 Moments of the cluster size distribution

The average cluster size is of course given by

$$\langle n \rangle = \sum_{n=1}^{\infty} n r(n), \quad (4.14)$$

but can actually be calculated even without knowledge of the cluster size distribution [90] as $\langle n \rangle = 2/(2 - \langle n_b \rangle)$, where $\langle n_b \rangle$, the average number of bonds per OH-group is given by

$$\begin{aligned}
 \langle n_b \rangle &= \\
 &= 0 \times (1 - p_H)p_0 \\
 &+ 1 \times [(1 - p_H)p_1 + p_H p_0] \\
 &+ 2 \times [p_H p_1 + (1 - p_H)p_2] \\
 &+ 3 \times p_H p_2 = \\
 &= 2p_H,
 \end{aligned} \tag{4.15}$$

so that

$$\langle n \rangle = \sum_{n=1}^{\infty} nr(n) = \frac{1}{1 - p_H} = \frac{1}{1 - p_A - p_{APB}}. \tag{4.16}$$

A more general approach to calculate the moments is to make use of the probability generating function

$$\hat{r}(z) = \langle z^n \rangle = \sum_{n=1}^{\infty} r(n)z^n, \tag{4.17}$$

applied to the recursive formula for $r(n)$:

$$\begin{aligned}
 \hat{r}(z) &= \sum_{n=1}^{\infty} \delta_{n,1} r(1)z^n + p_1 \sum_{n=1}^{\infty} r(n-1)z^n + p_2 \sum_{n=1}^{\infty} \sum_{k=1}^{\infty} r(k)r(n-k-1)z^n \\
 &= zr(1) + zp_1 \sum_{n=1}^{\infty} r(n-1)z^{n-1} + zp_2 \sum_{k=1}^{\infty} r(k)z^k \sum_{n=1}^{\infty} r(n-k-1)z^{n-k-1} \\
 &= zr(1) + zp_1 \hat{r}(z) + zp_2 [\hat{r}(z)]^2.
 \end{aligned} \tag{4.18}$$

The moments can be calculated by noting that the i th derivative of $\hat{r}(z)$ evaluated at $z = 1$ gives the i th factorial moment

$$\left(\frac{d}{dz} \hat{r}(z) \right)^i \Big|_{z=1} = \sum_{n=1}^{\infty} n(n-1) \dots (n-i+1) r(n) = \langle n(n-1) \dots (n-i+1) \rangle. \tag{4.19}$$

That the probability distribution $r(n)$ is normalised, i.e. that the zeroth moment is 1, is verified by substituting $z = 1$ and $\hat{r}(1) = 1$ in equation (4.18)

$$1 = p_0 + p_1 + p_2 = 1 - p_A + p_A - p_{APB} + p_{APB} \tag{4.20}$$

For $\langle n \rangle$ we get

$$\begin{aligned}
 \langle n \rangle &= \left. \frac{d}{dz} \hat{r} \right|_{z=1} = \left(p_0 + p_1 \hat{r}(z) + z p_1 \hat{r}'(z) + p_2 [\hat{r}(z)]^2 + 2z p_2 \hat{r}(z) \hat{r}'(z) \right) \Big|_{z=1} \\
 &= p_0 + p_1 + p_1 \langle n \rangle + p_2 + 2p_2 \langle n \rangle \\
 &\Leftrightarrow \\
 \langle n \rangle &= \frac{1}{1 - p_1 - 2p_2} = \frac{1}{1 - p_A - p_{APB}} \tag{4.21}
 \end{aligned}$$

in agreement with equation (4.16). The second factorial moment becomes

$$\begin{aligned}
 \langle n(n-1) \rangle &= \langle n^2 \rangle - \langle n \rangle = \left. \frac{d^2}{dz^2} \hat{r}(z) \right|_{z=1} \\
 &= \left(2p_1 \hat{r}'(z) + z p_1 \hat{r}''(z) + 4p_2 \hat{r}(z) \hat{r}'(z) + 2z p_2 ([\hat{r}'(1)]^2 + \hat{r}(1) \hat{r}''(1)) \right) \Big|_{z=1} \\
 &= 2p_1 \langle n \rangle + p_1 \langle n^2 \rangle - p_1 \langle n \rangle + 4p_2 \langle n \rangle + 2p_2 (\langle n \rangle^2 + \langle n^2 \rangle - \langle n \rangle) \\
 &\Leftrightarrow \\
 \langle n^2 \rangle &= \frac{2p_2 \langle n \rangle^2 + (1 + p_1 + 2p_2) \langle n \rangle}{1 - p_1 - 2p_2} \\
 &= 2p_2 \langle n \rangle^3 + (1 + p_1 + 2p_2) \langle n \rangle^2 \tag{4.22}
 \end{aligned}$$

so that the variance of $r(n)$ becomes

$$\langle n^2 \rangle - \langle n \rangle^2 = 2p_2 \langle n \rangle^3 + (p_1 + 2p_2) \langle n \rangle^2. \tag{4.23}$$

In Paper I, the variance is derived in a different way and is shown to be $\langle n^2 \rangle - \langle n \rangle^2 = -\langle n \rangle + 2(1 - p_A) \langle n \rangle^3$ which is equivalent to equation (4.23).

4.2 A quantitative model for the transient chain dynamics in alcohols

Even though the H-bonded clusters can be branched, the majority of experimental and computational work on alcohols, point towards chain-like structures with a low probability of branching, $p_B < 10\%$ [14, 16–32, 91]. To simplify the formulation of a model for the chain dynamics, we thus start from the assumption of chain like clusters without branching ($p_B = 0$) or loops. The cluster size distribution, $r(n)$ is then just given by the probability of having $n - 1$ H-bonded molecules, followed by a non-bonded molecule

$$r(n) = p^{n-1}(1 - p), \tag{4.24}$$

where n is the cluster size and $p \equiv p_A$ is the probability of having an H-bond between two molecules. The probability distribution $r(n)$, which is a geometrical distribution with mean $\langle n \rangle = 1/(1-p)$ and variance $\sigma^2 = p\langle n \rangle^2$, is often referred to in the polymer literature as the Schulz-Flory-Anderson distribution [87].

To introduce dynamics into the model, we assume, as is done in the transient chain model proposed by Gainaru *et al.* [9], that monomers join and leave the clusters only at the chain ends, i.e. we ignore the possibility that chains break in the middle and we also ignore the possibility of two chains merging into one larger structure. This has some support from calculations, showing that H-bonds inside the chains are stronger, and thus less likely to break, than the bonds at the ends of the chains [38]. We also assume that the rate of monomers leaving the cluster, μ , and the rate of monomers joining the cluster, λ , are independent of cluster size, n . The master equation describing the dynamics is then

$$\begin{aligned}\dot{s}(1|n_0) &= \mu s(2|n_0) - \lambda s(1|n_0) \\ \dot{s}(n|n_0) &= \mu s(n+1|n_0) + \lambda s(n-1|n_0) - (\mu + \lambda)s(n|n_0),\end{aligned}\tag{4.25}$$

where the dot denotes differentiation with respect to time, and $s(n|n_0) \equiv s(n, t|n_0, 0)$ is the probability that the cluster will contain n molecules at time t , given that it contained n_0 molecules at time 0. In general we will let s denote time dependent probabilities and r stationary, equilibrium probabilities. The first line of (4.25) ensures that the clusters have a positive size, $n > 0$. The general stationary distribution, $r(n) = \lim_{t \rightarrow \infty} s(n|n_0)$, for such a process can be shown to be [92]

$$r(n) = \frac{\lambda^{n-1}}{\mu^{n-1}} r(1),\tag{4.26}$$

where $r(1)$ is determined from requiring the probability distribution to be normalised to one. For the theory to be consistent, equations (4.24) and (4.26) must agree, and the ratio of molecules joining the cluster and molecules leaving the cluster must consequently be equal to the bonding probability

$$p = \frac{\lambda}{\mu}.\tag{4.27}$$

This condition is also equivalent to the condition of detailed balance [92]. Equation (4.25) also describes other scenarios, such as an asymmetric random walk on the positive half line [93], or a so called M/M/1-queue, with customers arriving at a rate λ and leaving at rate μ [94, 95] (with the difference that the queue size ≥ 0 , while the cluster sizes are > 0). In queuing theory, the ratio $p = \lambda/\mu$ is referred to as the traffic intensity. If the traffic intensity equals or exceeds 1, the queue size goes to infinity, which agrees intuitively with the interpretation as a bonding probability in the case of H-bonded chains of alcohol molecules.

In Paper IV, we adopt the assumption of Gainaru *et al.* [9], that the rates of monomers joining and leaving the clusters, λ , and μ , are similar to the α -relaxation rate as measured by dielectric spectroscopy. More specifically, when we fit the dielectric Debye peak, we assume that λ is exactly equal to the peak frequency of the dielectric α -relaxation. We conclude that the ratio of the two rates, i.e. p , increases slowly with decreasing temperature, which means that the two rates have very similar temperature dependencies, but that λ decreases slightly slower than μ .

The solution to equation (4.25) is known to be [93, 96]

$$s(n|n_0) = \kappa^{n-n_0} e^{-Kt\lambda\kappa^{-1}} \left(I_{n-n_0}(2t\lambda\kappa^{-1}) + \kappa^{-1} I_{n+n_0-1}(2t\lambda\kappa^{-1}) + (\kappa^{-1} - \kappa) \sum_{j=1}^{\infty} \kappa^{-j} I_{n+n_0-1+j}(2t\lambda\kappa^{-1}) \right), \quad (4.28)$$

where $\kappa = \sqrt{p}$, $K = \kappa + \kappa^{-1}$, and $I_m(t) = 1/\pi \int_0^\pi d\theta e^{t \cos \theta} \cos m\theta$ are modified Bessel functions of the first kind.

For numerical purposes, it is more convenient to use the integral representation [94]

$$s(n|n_0) = \delta_{n,n_0} - \frac{\lambda}{\pi} \kappa^{n-n_0-2} \int_0^{2\pi} \frac{F(\theta)}{\nu} (1 - e^{-\nu t}) d\theta, \quad (4.29)$$

with

$$F(\theta) = (\sin[n_0 - 1]\theta - \kappa \sin n_0\theta) (\sin[n - 1]\theta - \kappa \sin n\theta), \quad (4.30)$$

and $\nu = \lambda\kappa^{-1}(K - 2 \cos \theta)$.

Other interesting properties derived in the queueing theory literature is the “busy period of server” which translates to lifetime of a cluster, i.e. the time spent from that two monomers joins to become a cluster of size two, until the cluster has size one again. The probability distribution for the lifetime is given by

$$p(t) = \frac{1}{t\kappa} e^{-Kt\lambda\kappa^{-1}} I_1(2t\lambda\kappa^{-1}), t > 0 \quad (4.31)$$

with average $\langle t \rangle = 1/(\mu - \lambda) = p\langle n \rangle/\lambda$ [95]. The average “response time”, i.e. the average time a molecule spends in the cluster is given by Little’s law [97] as $\langle t_{\text{OH}} \rangle = \langle n \rangle/\lambda$, and if we identify λ with the α -relaxation time ($\lambda = 1/\tau_\alpha$), we obtain

$$\langle n \rangle = \frac{\langle t_{\text{OH}} \rangle}{\tau_\alpha}. \quad (4.32)$$

which was used in [9] to estimate average sizes of H-bonded 1-butanol clusters from dielectric- and NMR measurements.

4.2.1 The dipole moment distribution

Given the time dependent distribution, $s(n|n_0)$, the time dependent probability, $s(D|D_0) \equiv s(D, t|D_0, 0)$, of the cluster having dipole moment D at time t , given that it had dipole moment D_0 at time 0, can be expressed using the chain rule of probabilities as

$$\begin{aligned} s(D|D_0) &= \sum_{n_0=0}^{\infty} \sum_{n=0}^{\infty} \frac{s(D|n, D_0, n_0)s(n|n_0, D_0)r(D_0|n_0)r(n_0)}{r(D_0)} \\ &= \sum_{n_0=0}^{\infty} \sum_{n=0}^{\infty} \frac{s(D|n, D_0, n_0)s(n|n_0)r(D_0|n_0)r(n_0)}{r(D_0)} \end{aligned} \quad (4.33)$$

where we have assumed that $s(n|n_0, D_0) = s(n|n_0)$, i.e. n is conditionally independent of D_0 given n_0 .

For the case of straight chains consisting of monomers with dipole moment D_1 , the cluster dipole moment is uniquely given by n , i.e.

$$s(D|n, D_0, n_0) = r(D|n) = \delta(D - nD_1) \quad (4.34)$$

and $r(D_0|n_0) = \delta(D_0 - n_0D_1)$. The stationary dipole moment distribution is in this case given by $r(D) = p^{D/D_1}(1 - p) = r(n)$, with average $\langle D \rangle = D_1 \langle n \rangle$, and equation (4.33) becomes identical to the time dependent cluster size distribution

$$s(D|D_0) = s(n|n_0) \quad (4.35)$$

4.2.2 The dipole moment autocorrelation function

The (auto-) correlation function of the dipole moment distribution is defined as

$$C(t) \equiv \frac{\langle DD_0 \rangle - \langle D \rangle^2}{\langle D^2 \rangle - \langle D \rangle^2}, \quad (4.36)$$

where the time dependent part is more explicitly given by

$$\langle DD_0 \rangle = \int_0^\infty \int_0^\infty DD_0 s(D|D_0) r(D_0) dD_0 dD. \quad (4.37)$$

For the case of straight chains, we can insert equation 4.35 to obtain

$$\begin{aligned} \langle DD_0 \rangle &= \sum_{n_0=0}^{\infty} \sum_{n=0}^{\infty} nn_0 s(n|n_0) r(n_0) \\ &= D_1^2 \langle nn_0 \rangle. \end{aligned} \quad (4.38)$$

In the expression for $C(t)$, the monomer dipole moments cancel so that the dipole moment correlation function is identical to the cluster size correlation function $C_n(t)$. The time dependent part of $C_n(t)$ can be found in the queueing theory literature [94] and is given by

$$\langle nn_0 \rangle = \langle n \rangle^2 + 2\mu^2 p \langle n \rangle \frac{1}{\pi} \int_0^\pi d\theta \frac{\sin^2 \theta}{\nu^3} e^{-\nu t}, \quad (4.39)$$

with $\nu = \mu(1+p) - 2\mu\sqrt{p} \cos \theta = \mu\kappa(K - 2 \cos \theta)$. By inverting $\nu(\theta)$ with respect to θ we can eliminate θ . The integration limits become $\nu_{\min} = \mu(1+p - 2\sqrt{p})$ and $\nu_{\max} = \mu(1+p + 2\sqrt{p})$, and for $C(t)$ we get

$$C(t) = \int_{\nu_{\min}}^{\nu_{\max}} f(\nu) e^{-\nu t} d\nu, \quad (4.40)$$

with

$$f(\nu) = \frac{\mu}{2p\langle n \rangle^3} \frac{1}{\pi} \frac{\sqrt{4\mu\nu - (\mu/\langle n \rangle + \nu)^2}}{\nu^3}. \quad (4.41)$$

The power spectrum is

$$\hat{C}(\omega) \equiv 4 \int_0^\infty C(t) \cos \omega t \quad dt = 4 \int_{\nu_{\min}}^{\nu_{\max}} f(\nu) \frac{\nu}{\nu^2 + \omega^2} d\nu, \quad (4.42)$$

and hence the response function becomes

$$\chi(\omega) = \omega \hat{C}(\omega) = 4 \int_{\nu_{\min}}^{\nu_{\max}} f(\nu) \frac{\omega\nu}{\nu^2 + \omega^2} d\nu. \quad (4.43)$$

From equations (4.40) and (4.43) we see that the correlation function and its corresponding response function are integrals over exponential relaxations. We thus expect a stretched exponential behaviour, rather than a single exponential, Debye-type relaxation. In Paper IV, however, we show that the model fits the dielectric Debye peak rather well, and that the bonding probability p , and the average cluster sizes $\langle n \rangle = 1/(1-p)$ are in reasonable agreement with our results based on neutron diffraction. By allowing the chains to be curved, as suggested by the neutron diffraction results, as well as rotational diffusion of the clusters, the agreement is improved further.

5

Neutron Scattering

5.1 Probing the Structure using neutron diffraction

As mentioned in the introduction, physicist are mainly interested in four quantities; time, energy, position and momentum. In this chapter it will be explained how the change of momentum that a neutron suffers as it passes through a piece of material, in my case, liquid 1-propanol, can tell us about the relative positions of the atoms in the material. To see how, it is important to remember that neutrons, just like light, have a dual nature; they behave both as particles and waves. In diffraction experiments, it is interference effects caused by the neutrons' wave properties that are most important. The neutron impinging on a piece of material is thus typically modelled as a plane wave,

$$\psi = \psi_0 e^{i(\mathbf{k}_i \cdot \mathbf{r} - \omega_i t)}, \quad (5.1)$$

moving in the direction of a wavevector $\mathbf{k}_i = (0, 0, 2\pi/\lambda)$, where λ is the wavelength of the wave and ω_i is its angular frequency. The wavevector is related to the momentum and energy of the neutron through [98]

$$\mathbf{p}_i = \hbar \mathbf{k}_i, \quad (5.2)$$

and

$$E_i = \hbar \omega_i = \frac{\hbar^2 |\mathbf{k}_i|^2}{2m_n}, \quad (5.3)$$

where \hbar is Planck's constant, and $m_n = 1.67 \times 10^{-27}$ kg, is the mass of the neutron.

When the neutron hits the material, three things can happen: it can be absorbed, transmitted, or scattered. Due to the interaction between the neutron and the nuclei of the material, the scattered neutron will in general have a different

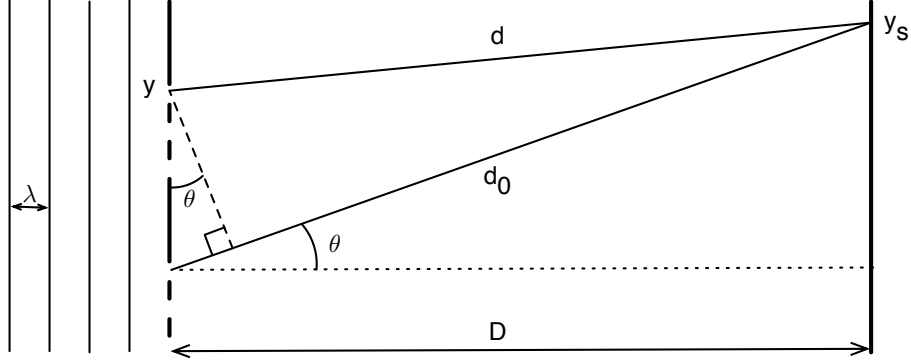


Figure 5.1: A Fraunhofer diffraction experiment: a plane wave is scattered through a number of slits and a diffraction pattern emerges on a screen far away from the slits

energy, E_f , as well as a different momentum, $\mathbf{p}_f = \hbar \mathbf{k}_f$, than it had before the scattering process. The change in momentum, or equivalently the change in wavevector, $\mathbf{Q} = \mathbf{k}_i - \mathbf{k}_f$, contains information about the positions of the atoms in the material.

To illustrate the relationship between the intensity of a scattered wave and the scattering system, let's first consider a simple, one dimensional example [99], illustrated in figure 5.1. A plane, one dimensional wave, with amplitude $\psi = \psi_0 e^{i(kx - \omega t)}$, moving in the positive x -direction, passes through a pattern of slits, located in the $x = 0$ plane and described by the aperture function $A(y)$, which takes on a value of one where there is a slit and is zero otherwise. After the wave has passed through the slits, it continues and hits a screen at $x = D$, far away from the slits. The amplitude of the wave hitting the screen at (D, y_s) will have contributions from all points in all slits the wave has passed through. To find the phase of all such contributions, the distance d , from the slit at point $(0, y)$ to the screen (D, y_s) has to be calculated. Applying the law of cosines and using $\sqrt{1+x} = 1 + x/2 + \mathcal{O}(x^2)$ results in

$$\begin{aligned}
 d &= \sqrt{d_0^2 + y^2 - 2d_0y \cos(\pi/2 - \theta)} \\
 &= d_0 \left(1 + \frac{y^2}{2d_0^2} - \frac{y}{d_0} \sin \theta \right) \\
 &= d_0 - y \sin \theta + \mathcal{O}(y^2/d_0)
 \end{aligned} \tag{5.4}$$

where the term of order $y^2/d_0 < y^2/D$ can be neglected as long as the Fraunhofer condition

$$\frac{y^2}{D} \ll \lambda, \tag{5.5}$$

is satisfied [100]. The path length is thus given by $d = d_0 - y \sin \theta$, and summing up the contributions from all the slits, we finally get

$$\begin{aligned}\psi &= \psi_0 e^{i(kd_0 - \omega t)} \int_{-\infty}^{\infty} A(y) e^{-iky \sin \theta} dy \\ &= \psi_0 e^{i(kd_0 - \omega t)} \int_{-\infty}^{\infty} A(y) e^{-iQy} dy \\ &= \psi_0 e^{i(kd_0 - \omega t)} \hat{A}(Q)\end{aligned}\quad (5.6)$$

where $\hbar Q = \hbar k \sin \theta$ is the y -component of the momentum change $\hbar \mathbf{Q} = \hbar \mathbf{k}_i - \hbar \mathbf{k}_f$, and $\hat{A}(Q)$ is the Fourier transform of $A(y)$. If we could measure the wave function ψ directly, we could calculate the inverse Fourier transform, and obtain the position and size of the slits through the aperture function $A(y)$. Unfortunately, what we measure is the intensity, I , on the screen, which is proportional to the amplitude squared

$$\begin{aligned}I(Q) &\propto |\psi|^2 = \psi_0^2 \left| \hat{A}(Q) \right|^2 \\ &= \psi_0^2 \int_{-\infty}^{\infty} \left(\int_{-\infty}^{\infty} A(y) A(y + y') dy' \right) e^{iQy} dy.\end{aligned}\quad (5.7)$$

The last equality uses the relationship between a convolution and its Fourier transform, and shows that the intensity is the Fourier transform of the auto-correlation function of the aperture function $A(y)$. From the measured intensity one can thus perform an inverse Fourier transform and get the autocorrelation function of $A(y)$. Unfortunately, there is not a one-to-one relationship between a function and its autocorrelation function, so additional information is required to fully recover the aperture function $A(y)$.

The step from the simple slit experiment described above to a (idealised) neutron diffraction experiment, where neutrons are scattered from a collection of atoms, figure 5.2, is rather straight forward: In the slit experiment, each point within a slit can be seen as a point source radiating circular waves, whose amplitudes are then summed up at the screen. In a neutron diffraction experiment, the slits are replaced by the atoms' nuclei, also acting as point sources, from which the scattered neutrons emanate as spherical waves. Furthermore, the ‘‘aperture function’’ does not only take on values of one or zero, but instead it takes on different values, b_i , depending on the composition of the nuclei, i.e. atom type, isotope, and also nuclear spin. The aperture function, or interaction potential, of a sample consisting of N atoms can thus be written [101]

$$A(\mathbf{r}) = \frac{2\pi\hbar^2}{m_n} \sum_{i=1}^N b_i \delta(\mathbf{r} - \mathbf{r}_i), \quad (5.8)$$

where b_i is called the neutron scattering length of atom i , and the prefactor $\frac{2\pi\hbar^2}{m_n}$ makes sure that the total scattering from a single nucleus with index i , is exactly b_i .

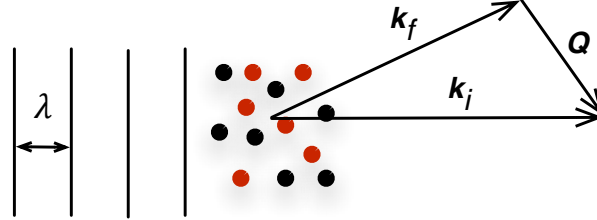


Figure 5.2: Neutrons with incident wavevector \mathbf{k}_i are scattered by the atoms in the sample. The scattered neutrons have wavevector $\mathbf{k}_f = \mathbf{k}_i - \mathbf{Q}$, where $\hbar\mathbf{Q}$ is the momentum transferred during the scattering event, from the neutron to the sample.

The resulting scattered wave function thus becomes

$$\begin{aligned}
 \psi(\mathbf{Q}) &= \psi_0 e^{-i\omega t} \int \int \int A(\mathbf{r}) e^{i\mathbf{Q}\cdot\mathbf{r}} d^3\mathbf{r} \\
 &= \psi_0 e^{-i\omega t} \hat{A}(\mathbf{k}) \\
 &= \psi_0 e^{-i\omega t} \frac{2\pi\hbar^2}{m_n} \sum_{i=1}^N b_i e^{i\mathbf{Q}\cdot\mathbf{r}}, \tag{5.9}
 \end{aligned}$$

where the one dimensional integral in equation (5.6) has been replaced by its three dimensional counterpart. Again, if we could measure the wave function directly, we could do an inverse Fourier transform and get the position of all the atoms. What we measure is instead the differential scattering cross section,

$$\begin{aligned}
 \frac{d\sigma}{d\Omega} &= \left(\frac{m_n}{2\pi\hbar^2\psi_0^2} \right)^2 \langle |\psi(\mathbf{Q})|^2 \rangle \\
 &= \sum_{i=1}^N \sum_{j=1}^N \overline{b_i b_j} \langle e^{i\mathbf{Q}\cdot\mathbf{r}_i} e^{-i\mathbf{Q}\cdot\mathbf{r}_j} \rangle, \tag{5.10}
 \end{aligned}$$

which is the fraction of neutrons scattered into a solid angle Ω . Over the course of the experiment, the atoms in the sample will move around, and this is reflected in the angular brackets, denoting a thermal average of the atom positions. The bar over the scattering lengths denote an average over isotopes and spin states of the different nuclei.

Equation (5.10) can be interpreted in terms of the partial pair correlation functions [101], $g_{\alpha\beta}(\mathbf{r})$, defined analogously to the molecular pair distribution

function in equation (2.4)

$$N\rho c_\alpha c_\beta g_{\alpha\beta}(r) = \sum_{i=1}^{N_\alpha} \sum'_{j=1}^{N_\beta} \langle \delta(\mathbf{r} + \mathbf{R}_i - \mathbf{R}_j) \rangle, \quad (5.11)$$

where $\rho = N/V$ is the number density of the liquid, $c_\alpha = N_\alpha/N$ is the concentration of atomic species α and the prime on the second sum means that terms with $i = j$ are excluded if $\alpha = \beta$. From $g_{\alpha\beta}(r)$ the partial structure factors are defined as

$$S_{\alpha\beta}(Q) = c_\alpha \delta_{\alpha\beta} + c_\alpha c_\beta \rho \int d\mathbf{r} e^{i\mathbf{Q}\cdot\mathbf{r}} (g_{\alpha\beta}(r) - 1), \quad (5.12)$$

and equation (5.10) becomes

$$\frac{d\sigma}{d\Omega} = N \sum_{\alpha} c_{\alpha} \left(\overline{b_{\alpha}^2} - \overline{b_{\alpha}}^2 \right) + N \sum_{\alpha} \sum_{\beta} \overline{b_{\alpha}} \overline{b_{\beta}} S_{\alpha\beta}(Q), \quad (5.13)$$

i.e. the differential scattering cross section is a sum of a Q -independent background, called the incoherent cross section, plus a weighted sum of the partial structure factors, called the coherent cross section.

In the literature, it is usually not the differential scattering cross section that is reported, but instead either the total interference function [102],

$$F(Q) = \sum_{\alpha} \sum_{\beta} \overline{b_{\alpha}} \overline{b_{\beta}} (S_{\alpha\beta}(Q) - 1), \quad (5.14)$$

or the normalised, neutron weighted, total structure factor, given by

$$S(Q) = \frac{\sum_{\alpha} \sum_{\beta} \overline{b_{\alpha}} \overline{b_{\beta}} (S_{\alpha\beta}(Q) - 1)}{\sum_{\alpha} c_{\alpha} \langle \overline{b_{\alpha}} \rangle^2} + 1. \quad (5.15)$$

Examples of $F(Q)$ for Propanol, Butanol, Propylene Glycol, and Glycerol are shown in figure 5.3. The main peak, at $Q \approx 1.4 \text{ \AA}^{-1}$, corresponding to distances $2\pi/Q \approx 4.5 \text{ \AA}$, comes mainly from the intermolecular separation, i.e. from the density of the liquids. The contributions at higher values of momentum transfer, Q , is mainly due to intramolecular correlations.

The partial pair distribution functions, $g_{\alpha\beta}(r)$, and thus the partial structure factors, $S_{\alpha\beta}(Q)$ give the distribution of α atoms around β atoms and vice versa. If there are m atom types in our liquid, there are $m(m+1)/2$ partial structure factors, and to obtain them all experimentally one has to perform measurements on equally many samples with different isotopic composition. In practise, because of the low availability of neutron beam time, this is only possible for the simplest of liquids, such as water. To compensate for the incomplete information obtained in the diffraction experiment, one can use information obtained from

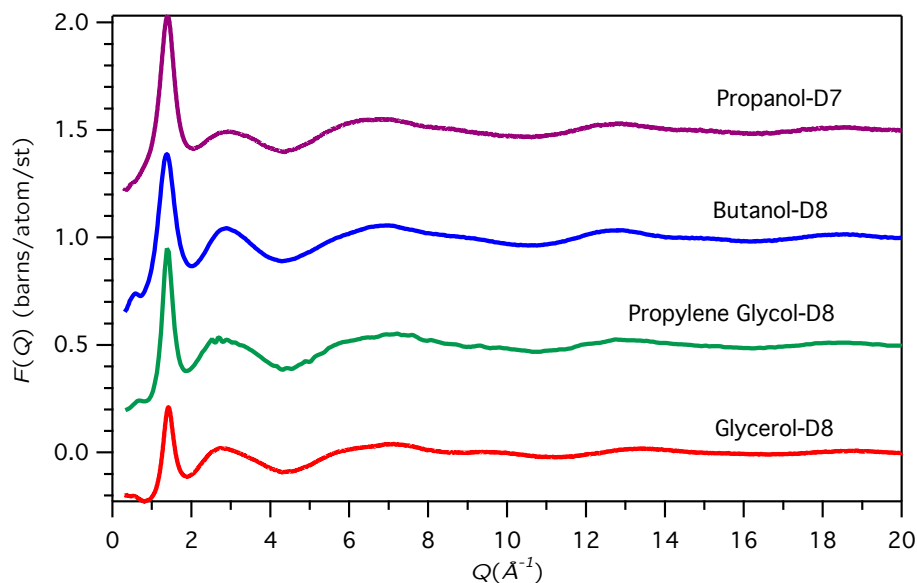


Figure 5.3: Total interference functions, $F(Q)$, for four of the alcohols in Paper I

other techniques when analysing the data. For molecular liquids, the intramolecular structure is usually known quite well from, e.g., quantum mechanical calculations, and this information can be used in conjunction with the diffraction data when performing a so called EPSR simulation described in the next chapter.

The diffraction measurements in this work was done using the NIMROD instrument at the ISIS spallation source in the U.K. The sample was put in a flat Titanium-Zirconium can with dimensions 5 cm by 5 cm by 0.1 cm, which was then inserted into a cryostat used to control the temperature of the sample. The sample thickness of 0.1 cm should give a scattering probability of about 10%, and thus unwanted multiple scattering should occur with as little as 1% probability. The Titanium-Zirconium alloy, with proportions 2.1:1, has a coherent cross section very close to zero, and is thus transparent to neutrons. To obtain the differential scattering cross section on an absolute scale, Vanadium, which scatters almost completely incoherently, is used for normalisation.

5.2 Probing dynamics using QENS and NSE

In section 5.1, the atomic coordinates \mathbf{R}_i were assumed to be time independent. This is of course not true, especially not in a liquid, but as long as the energy transfer from the neutron to the sample is small, it is a reasonable approximation known as the static approximation [99]. If, on the other hand, we can measure the energy transfer, we can obtain information about the motion of the atoms in the

sample. This is what is accomplished by the techniques of quasi elastic neutron scattering (QENS) and Neutron Spin Echo (NSE), which will be described here.

5.2.1 Quasi elastic neutron scattering

What makes inelastic scattering different from the elastic counterpart is that the magnitude of the momentum, and hence the energy, changes during the scattering event. The change in energy is given by [103]

$$E = \hbar\omega = \frac{\hbar^2|\mathbf{k}_i|^2}{2m_n} - \frac{\hbar^2|\mathbf{k}_f|^2}{2m_n} = \frac{\pi\hbar}{m_n} \left(\frac{1}{\lambda_i^2} - \frac{1}{\lambda_f^2} \right). \quad (5.16)$$

What we measure is now the partial differential cross section

$$\frac{\partial^2\sigma}{\partial\Omega\partial\omega} = \frac{k_i}{k_f} \frac{1}{2\pi} \sum_i \sum_j \int_{-\infty}^{\infty} \bar{b}_\alpha \bar{b}_\beta \langle e^{i\mathbf{Q}\cdot\mathbf{R}_i(t)} e^{i\mathbf{Q}\cdot\mathbf{R}_j(0)} \rangle e^{-i\omega t} dt, \quad (5.17)$$

which is related to the differential cross section through

$$\frac{d\sigma}{d\Omega} = \int_0^\infty \frac{\partial^2\sigma}{\partial\Omega\partial\omega} d\omega. \quad (5.18)$$

The partial differential cross section is essentially the space-time Fourier transform of the van Hove correlation function $G(\mathbf{r}, t)$

$$\frac{\partial^2\sigma}{\partial\Omega\partial\omega} \propto S(Q, \omega) \propto \frac{k_i}{k_f} \int \int G(\mathbf{r}, t) e^{i(\mathbf{Q}\cdot\mathbf{r} - \omega t)} d^3\mathbf{r} dt, \quad (5.19)$$

where $G(\mathbf{r}, t)$ is defined similarly to the radial distribution function (2.4):

$$G(\mathbf{r}, t) = \left\langle \frac{1}{N} \sum_{i=1}^N \sum_{j=1}^N \delta(\mathbf{r} - \mathbf{r}_j(t) + \mathbf{r}_i(0)) \right\rangle. \quad (5.20)$$

The van Hove correlation function contains information about correlation in time as well as space. It will thus tend to be peaked around values of \mathbf{r} corresponding to units moving together in the liquid, such as neighbouring molecules, or clusters of molecules. For all values of \mathbf{r} , it will decay with respect to time as the molecules move in a diffusive manner.

The QENS measurement presented in Paper V were performed on the time focusing time of flight spectrometer IN6 at the Institute Laue Langevin (ILL), Grenoble, France, which is shown in figure 5.4. The instrument first filters out three beams, containing neutrons of three distinct wave vectors, using Bragg scattering from graphite crystals. The continuous flow of neutrons is turned into

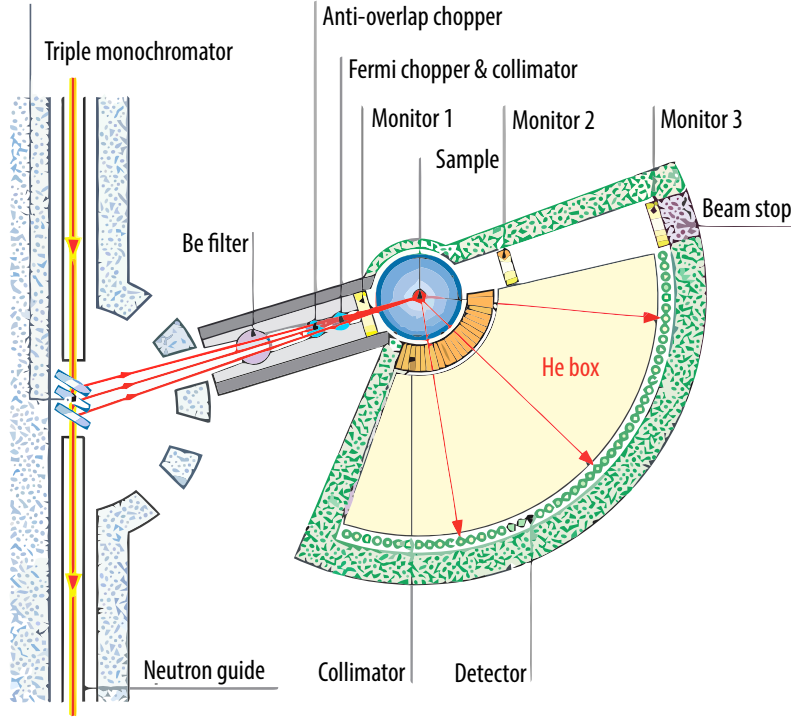


Figure 5.4: The time focusing time of flight spectrometer IN6. Image courtesy of the ILL, www.ill.eu

short pulses by a rotating anti-overlap chopper, and then passes through a Fermi chopper, that lets through the slower neutrons first to make sure all neutrons end up on the detector simultaneously a known period of time later, as long as the scattering is fully elastic. Since energy exchange can take place in the sample however, the time focusing is partially lost, and the time difference between the elastically and inelastically scattered neutrons can then be used to determine the change in velocity, and thus the energy transfer through equation (5.16) and the relation between momentum, wave vector, and velocity $\mathbf{p} = \hbar\mathbf{k} = m_n\mathbf{v}$.

5.2.2 Neutron spin echo

While QENS measures the dynamic structure factor $S(Q, \omega)$, neutron spin echo measures the intermediate scattering function

$$I(Q, t) \propto \int G(\mathbf{r}, t) e^{i\mathbf{Q}\cdot\mathbf{r}} d\mathbf{r} \propto \frac{1}{2\pi} \int S(Q, \omega) e^{i\omega t} d\omega \quad (5.21)$$

directly through a clever trick involving the neutrons' spin [103, 104]. To achieve this in the NSE instrument IN11 at ILL (see figure 5.5), the neutrons are first

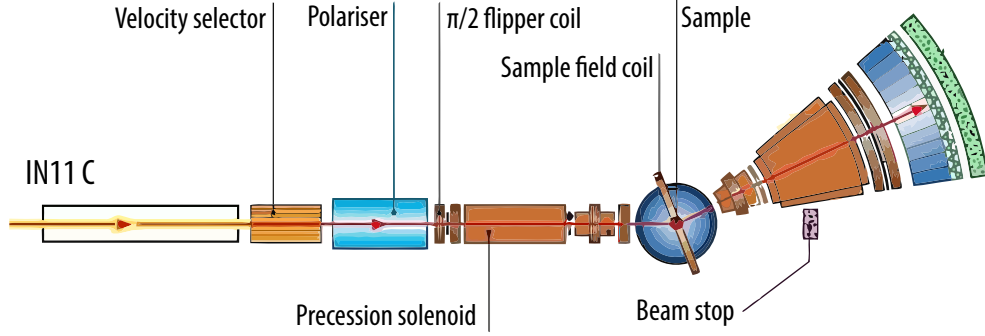


Figure 5.5: The neutron spin echo instrument IN11C. Image courtesy of the ILL

monochromatised to a narrow range, $\lambda_0 \pm 10\%$, by a rotating helical velocity selector. The beam is then polarised longitudinally by a pair of 60 cm long supermirrors mounted 1 cm apart inside a solenoid. A $\pi/2$ -flipper then flips the spins to make a transversally polarised beam. The neutrons are then made to precess inside a solenoid containing a magnetic field, perpendicular to the polarisation of the beam. If the magnetic field has strength H_0 , the precession angle after traveling a distance l inside the solenoid is

$$\phi = \gamma_n \frac{lH_0}{v}, \quad (5.22)$$

where v is the velocity and $\gamma_n = 1.83e8 \text{ Hz T}^{-1}$ is the gyromagnetic ratio of the neutron. A π flipper just before the sample flips the spins 180° into their mirror image, and then after passing the sample, the neutrons enter a second precession field with the same direction as the first one, and strength H_1 . Because of the π flipper, the second field re-phases the neutrons, which because of their different velocities became dephased inside the first solenoid. This only happens, however, as long as the scattering is completely elastic and doesn't affect the neutrons velocities. If the scattering is inelastic on the other hand, it can be shown [103, 104] that, as long as

$$\frac{l_0 H_0}{l_1 H_1} = \frac{\bar{v}_i^3}{\bar{v}_f^3}, \quad (5.23)$$

where \bar{v}_i and \bar{v}_f are the average initial and final neutron velocities, the final phase difference is approximately given by

$$\phi_1 - \phi_0 \approx \gamma_n \frac{H_1 l_1}{m_n v_f^3} \hbar \omega. \quad (5.24)$$

Noting that $t = \gamma_n \frac{H_1 l_1}{m_n v_f^3} \hbar$ has units of time, and that the distribution of ω is given by $S(Q, \omega)$, the measured average polarisation component can be expressed as

$$P_x = \langle \cos(\omega_1 - \omega_0) \rangle = \frac{\int S(Q, \omega) \cos(\omega_1 - \omega_0) d\omega}{\int S(Q, \omega) d\omega} = \frac{I(Q, t)}{I(Q, 0)}, \quad (5.25)$$

which is the normalised intermediate scattering function.

6

Raman Spectroscopy

When light hits a piece of material it will either be absorbed, transmitted or scattered. Most of the scattered light will be of the same wavelength as the incident light. This process is called Rayleigh scattering. The rest of the scattered light, which differs in wavelength from the incident light, provides information about the material, such as the frequencies and symmetries of molecular vibrations. This second process is called Raman scattering.

In my studies, the focus has primarily been on the vibrations of the hydroxyl (OH) groups present in water and alcohols. Because of the forces (so called hydrogen bonds) between OH-groups sitting on neighbouring molecules, the vibrational frequency of a molecule's OH group depends strongly on arrangement of the molecules in the local neighbourhood and vice versa. The local neighbourhood of a molecule can thus be investigated by measuring the vibrational frequency of a molecules OH group, e.g. using Raman spectroscopy.

6.1 Classical Theory of Raman Scattering

Some molecules, like water, are polar, i.e. they have a non-zero permanent dipole moment defined by

$$\mu_{\text{perm}} = \sum_k \mathbf{r}e. \quad (6.1)$$

Other molecules, like carbon dioxide, do not have a permanent dipole moment. As will be discussed later, symmetry plays a big role in determining how molecules scatter light, but already here we find a simple connection to symmetries. Molecules that have a centre of inversion, i.e. molecules that look identical if you negate all coordinates, do not have a permanent dipole moment, while molecules without a centre of inversion usually do have a permanent dipole moment.

Regardless of whether the molecule has a *permanent* dipole or not, a dipole moment will be *induced* if the molecule interacts with light. The induced dipole moment is

$$\mu_{\text{ind}} = \alpha \mathbf{E} + \dots, \quad (6.2)$$

where E is the electromagnetic field strength of the light and α is called the *polarisability* tensor of the molecule. The terms represented by the dots are higher order in \mathbf{E} and can be omitted as long as \mathbf{E} is sufficiently weak. The fact that the polarisability is a tensor means that the induced dipole need not be parallel with the incoming light represented by \mathbf{E} .

The electromagnetic field \mathbf{E} varies with time according to

$$\mathbf{E} = \mathbf{E}_0 \cos \omega_{\mathbf{E}} t = \frac{1}{2} \mathbf{E}_0 (e^{i\omega_{\mathbf{E}} t} + e^{-i\omega_{\mathbf{E}} t}), \quad (6.3)$$

where $\omega_{\mathbf{E}}$ is the angular frequency of the light. Since the atoms in a molecule vibrate around their equilibrium positions, also the polarisability tensor α has a time dependence. The vibrations are most conveniently described in terms of so called normal coordinates (more about normal coordinates and why they are convenient in the symmetry section 6.4). Assuming harmonic vibrations, which is sufficient if we are not interested in overtones and combination tones of the vibrational spectrum, the k th normal mode can be written as

$$Q_k = Q_{k0} \cos \omega_k t = \frac{1}{2} Q_{k0} (e^{i\omega_k t} + e^{-i\omega_k t}), \quad (6.4)$$

where Q_{k0} is the amplitude and ω_k is the angular frequency of the k th normal mode of vibration.

To describe the time dependence of the polarisability tensor we can expand its elements α_{ij} in terms of the normal coordinates Q_k .

$$\alpha_{ij} = (\alpha_{ij})_0 + \sum_k \left. \frac{\partial \alpha_{ij}}{\partial Q_k} \right|_{Q_k=0} Q_k + \dots \quad (6.5)$$

Neglecting higher order terms means that we, just as we did for the normal coordinates, use a harmonic approximation for the polarisability which, again, is sufficient if we do not care about overtones and combination tones in the vibrational spectrum. By defining the derived polarisability tensor α'_k as the tensor having elements

$$(\alpha'_{ij})_k = \left. \frac{\partial \alpha_{ij}}{\partial Q_k} \right|_{Q_k=0} \quad (6.6)$$

we can write the equation for the whole polarisability tensor as

$$\alpha = \alpha_0 + \sum_k \alpha'_k Q_k + \dots \quad (6.7)$$

Combining the equations for the induced dipole moment (6.2), the time dependence of the electric field (6.3), and the time dependence of the polarisability tensor (6.7) gives the time dependence of the induced dipole moment:

$$\begin{aligned}
 \mu_{\text{ind}} &= \alpha_0 \mathbf{E}_0 \cos \omega_{\mathbf{E}} t + \sum_k \alpha' Q_{k0} \mathbf{E}_0 \cos \omega_k t \cos \omega_{\mathbf{E}} t = \\
 &= \alpha_0 \mathbf{E}_0 \cos \omega_{\mathbf{E}} t \\
 &\quad + \sum_k \frac{1}{2} \alpha' Q_{k0} \mathbf{E}_0 \cos(\omega_{\mathbf{E}} - \omega_k) t \\
 &\quad + \sum_k \frac{1}{2} \alpha' Q_{k0} \mathbf{E}_0 \cos(\omega_{\mathbf{E}} + \omega_k) t,
 \end{aligned} \tag{6.8}$$

where the last equality can be easily proven using the complex forms of equations 6.3 and 6.4.

According to classical electrodynamics, a dipole with amplitude μ oscillating with a certain angular frequency ω will radiate light of that same frequency. The intensity of the light radiated at an angle θ from the axis of the dipole is given by the Larmor formula

$$I_{\text{tot}} = \frac{\omega^4 \mu^2 \sin^2 \theta}{32\pi^2 \varepsilon_0 c_0^3}, \tag{6.9}$$

where ε_0 is the vacuum permittivity and c_0 is the speed of light in vacuum. From equation (6.8) we thus see the induced dipole in our molecule will emit light of the same angular frequency ω as the incoming light, i.e. Rayleigh scattering, but it will also emit light with frequencies shifted by the frequencies of the molecular vibrations ω_k . The light with angular frequencies $\omega - \omega_k$ represent Stokes Raman scattering while the light with frequencies $\omega + \omega_k$ represent Anti-Stokes Raman scattering.

The classical analysis does not give us the strength of the Raman scattering, for that we have to resort to a quantum mechanical treatment, but it does tell us, that in order for Raman scattering to occur, the derived polarisability α' of the molecule, needs to be non-zero.

6.2 A Few Words About Units

In the previous section, as well as in the following sections, I used angular frequencies for the scattered light. The relation between the angular frequency ω and the frequency ν is

$$\omega = 2\pi\nu. \tag{6.10}$$

Both frequency and angular frequency have the unit 1/second, s^{-1} . Sometimes it is more convenient to use wavelength λ rather than frequency. The wavelength

in meters is given by

$$\lambda = c/\nu, \quad (6.11)$$

where $c = 299,792,458$ m/s is the speed of light. Spectroscopists also often use wavenumbers which have the unit inverse centimetres, cm^{-1} . Wavenumbers are usually denoted by $\tilde{\nu}$ and the relationships between wavenumber and the quantities above are given by

$$\tilde{\nu} = \frac{1}{100\lambda} = \frac{\nu}{100c} = \frac{\omega}{2\pi \cdot 100c}. \quad (6.12)$$

6.3 Quantum Theory of Raman Scattering

In the semi-quantum treatment of Raman scattering presented here, the light impinging on the sample is still treated as a classical electromagnetic wave, while the vibrating molecules are treated quantum mechanically. This compromise between classical and quantum mechanics has the advantage over the fully quantised field theoretical description of being more concise and readable, while still resulting in the same expression for the scattered radiation in terms of molecular properties.

6.3.1 Derivation of the General Polarisability Tensor

In going from the classical to the quantum description, one first has to exchange the dipole moments for dipole transition operators. The dipole transition operator is defined analogously to equation (6.1), $\hat{\mu} = \sum_k \mathbf{r} e$, but \mathbf{r} is now the quantum mechanical position operator. Similarly the induced dipole transition operator is completely analogous to equation (6.2)

$$\mu_{\text{ind}} = \alpha_{fi} \mathbf{E} + \dots, \quad (6.13)$$

where, again, the dots represent terms that are higher order in \mathbf{E} and α_{fi} is the induced transition polarisability operator for going from the initial state $|i\rangle$ to the final state $|f\rangle$. The interaction Hamiltonian for a dipole interacting with an electromagnetic field with field strength \mathbf{E} is simply

$$\hat{H} = -\boldsymbol{\mu} \cdot \mathbf{E}, \quad (6.14)$$

but to ensure the right initial condition [105], the Hamiltonian used in time-dependent perturbation theory to obtain the perturbed initial and final states is the slightly modified

$$\hat{H} = -\boldsymbol{\mu} \cdot \mathbf{E} e^{\eta t}, \quad (6.15)$$

where the extra factor $e^{\eta t}$ is used to turn the perturbation on slowly, or, as $\eta \rightarrow 0$, even adiabatically.

The perturbed quantum mechanical states $|i'\rangle$ of the molecules interacting with the electric field can be expressed as

$$|i'\rangle = |i^{(0)}\rangle + |i^{(1)}\rangle + \dots \quad (6.16)$$

and

$$|f'\rangle = |f^{(0)}\rangle + |f^{(1)}\rangle + \dots, \quad (6.17)$$

where $|i^{(0)}\rangle = |i\rangle$ represents the unperturbed stationary states of the molecule with energy E_i , $|i^{(1)}\rangle$ represents the first order correction (linear in the perturbing field \mathbf{E}) and so on, and similarly for the final state $|f'\rangle$. The first order correction can be expressed as

$$|i^{(1)}\rangle = \sum_r c_r^{(1)}(t)|r\rangle, \quad (6.18)$$

where $c_r^{(1)}(t)$, obtained through standard time dependent perturbation theory (see e.g. [105]), is given by

$$\begin{aligned} c_r^{(1)}(t) &= \frac{i}{\hbar} \int_{-\infty}^t e^{i\omega_{ri}t'} \langle r|\hat{\mu} \cdot \mathbf{E} e^{\eta t'} |i\rangle dt' \\ &= \frac{i}{\hbar} \langle r|\hat{\mu}|i\rangle \cdot \mathbf{E}_0 \int_{-\infty}^t e^{(i\omega_{ri} + \eta)t'} \frac{1}{2} (e^{i\omega_{\mathbf{E}}t'} + e^{-i\omega_{\mathbf{E}}t'}) dt' \\ &= \frac{1}{2\hbar} \langle r|\hat{\mu}|i\rangle \cdot \mathbf{E}_0 \left(\frac{e^{i(\omega_{ri} + \omega_{\mathbf{E}})t}}{\omega_{ri} + \omega_{\mathbf{E}} - i\eta} + \frac{e^{i(\omega_{ri} - \omega_{\mathbf{E}})t}}{\omega_{ri} - \omega_{\mathbf{E}} - i\eta} \right) e^{\eta t}, \end{aligned} \quad (6.19)$$

with $\omega_{ri} = (E_r - E_i)/\hbar$. From the perturbed states of the molecule, the first order dipole transition amplitude, linear in \mathbf{E} , is then obtained through

$$\mu_{fi}^{(1)} = \langle f^{(1)}|\hat{\mu}|i^{(0)}\rangle + \langle f^{(0)}|\hat{\mu}|i^{(1)}\rangle, \quad (6.20)$$

which, after getting rid of some insignificant terms (see [106] for details) and going to the adiabatic limit, $\eta \rightarrow 0$, gives

$$\begin{aligned} \mu_{\rho}^{(1)} &= \frac{1}{2\hbar} \sum_r \left(\frac{\langle f|\hat{\mu}_{\rho}|r\rangle \langle r|\hat{\mu}_{\sigma}|i\rangle}{\omega_{ri} - \omega_{\mathbf{E}}} + \frac{\langle f|\hat{\mu}_{\sigma}|r\rangle \langle r|\hat{\mu}_{\rho}|i\rangle}{\omega_{rf} + \omega_{\mathbf{E}}} \right) (E_0)_{\sigma} e^{-i(\omega_{\mathbf{E}} - \omega_{fi})t} \\ &+ \text{complex conjugate} \\ &= \frac{1}{2} \alpha_{fi} \mathbf{E}_0 (e^{-i(\omega_{\mathbf{E}} - \omega_{fi})t} + e^{i(\omega_{\mathbf{E}} - \omega_{fi})t}). \end{aligned} \quad (6.21)$$

Note that summation over the repeated index σ is implied.

The general expression for the components of the induced transition polarisability tensor is thus given by

$$\alpha_{\rho\sigma} = \frac{1}{\hbar} \sum_r \left(\frac{\langle f|\hat{\mu}_{\rho}|r\rangle \langle r|\hat{\mu}_{\sigma}|i\rangle}{\omega_{ri} - \omega_{\mathbf{E}}} + \frac{\langle f|\hat{\mu}_{\sigma}|r\rangle \langle r|\hat{\mu}_{\rho}|i\rangle}{\omega_{rf} + \omega_{\mathbf{E}}} \right) \quad (6.22)$$

For equation (6.22) to be valid, it is required that the frequency of the electric field corresponds to an energy (via $E = \hbar\omega$) that is much smaller than the difference between electronic levels, but much larger than the spacing of any vibrational modes (see [106] for a more detail derivation). This type of Raman scattering is termed "normal pure vibrational Raman-scattering", and for the transparent liquids in my studies, the condition is easily fulfilled using a standard green line (514.5 nm) from an Ar-ion laser.

6.3.2 Simplification of the Polarisability Tensor

The next step is to introduce enough approximations to make it feasible to actually calculate the matrix elements in equation (6.22). The first approximation is a classical one introduced by Born and Oppenheimer wherein one separates the electronic degrees of freedom from the vibrational and rotational degrees of freedom

$$|r\rangle = |e^r v^r R^r\rangle \approx |e^r\rangle |v^r\rangle |R^r\rangle, \quad (6.23)$$

where e^r , v^r and R^r are electronic, vibrational and rotational quantum numbers. Also the energy eigenvalues separate into

$$\omega_r = \omega_{e^r v^r R^r} \approx \omega_{e^r} + \omega_{v^r} + \omega_{R^r}. \quad (6.24)$$

It is usually a reasonable assumption that both the initial and final electronic states are the ground state with quantum number e^g . If further $\omega_{\mathbf{E}}$ is much larger than any vibrational frequencies, only the terms in equation (6.22), with $e^r \neq e^g$ are relevant. In these cases the rotational energy differences, $\omega_{R^r} - \omega_{R^i}$ and $\omega_{R^r} - \omega_{R^f}$, as well as the vibrational energy differences can be neglected compared to the electronic energy differences, so that $\omega_{r_i} \approx \omega_{e^r e^i}$ and $\omega_{r_f} \approx \omega_{e^r e^f}$. We can then apply the closure theorem

$$\sum_r |r\rangle \langle r| = 1, \quad (6.25)$$

to the vibrational and rotational states and equation (6.22) becomes

$$\alpha_{\rho\sigma} = \frac{1}{\hbar} \sum_{e^r \neq e^g} \left(\frac{\langle v^f | \langle e^g | \hat{\mu}_\rho | e^r \rangle \langle e^r | \hat{\mu}_\sigma | e^g \rangle | v^i \rangle}{\omega_{e^r e^g} - \omega_{\mathbf{E}}} + \frac{\langle v^f | \langle e^g | \hat{\mu}_\sigma | e^r \rangle \langle e^r | \hat{\mu}_\rho | e^g \rangle | v^i \rangle}{\omega_{e^r e^g} + \omega_{\mathbf{E}}} \right), \quad (6.26)$$

where I have also assumed that the rotational degrees of freedom can be neglected, which is certainly the case in my measurements. This simplified form of the polarisability tensor is referred to as the "Placzek pure vibrational polarisability tensor" [106], and can be conveniently rewritten as

$$\alpha_{\rho\sigma} = \langle v^f | \hat{\alpha}_{\rho\sigma}(\{Q_k\}) | v^i \rangle, \quad (6.27)$$

where

$$\hat{\alpha}_{\rho\sigma}(\{Q_k\}) = \frac{1}{\hbar} \sum_{e^r \neq e^g} \left(\frac{\langle e^g | \hat{\mu}_\rho | e^r \rangle \langle e^r | \hat{\mu}_\sigma | e^g \rangle}{\omega_{e^r e^g} - \omega_{\mathbf{E}}} + \frac{\langle e^g | \hat{\mu}_\sigma | e^r \rangle \langle e^r | \hat{\mu}_\rho | e^g \rangle}{\omega_{e^r e^g} + \omega_{\mathbf{E}}} \right), \quad (6.28)$$

can be shown [106] to be a function of the set of vibrational normal coordinates $\{Q_k\}$ only. Expanding $\hat{\alpha}_{\rho\sigma}$ as a Taylor series in Q_k finally gives a result we can make explicit use of

$$\alpha_{\rho\sigma} = \hat{\alpha}_{\rho\sigma} \Big|_{Q=0} \langle v^f | v^i \rangle + \sum_k \frac{\partial \hat{\alpha}_{\rho\sigma}}{\partial Q_k} \Big|_{Q=0} \langle v^f | Q_k | v^i \rangle + \dots \quad (6.29)$$

6.3.3 The Harmonic Oscillator Approximation

If the vibrational modes of the molecule can be approximated as harmonic oscillators we can write the total vibrational wave function, e.g. $|v^i\rangle$, as a product of the harmonic oscillator functions $|v_k^i\rangle$ of the individual modes

$$|v^i\rangle = \prod_k |v_k^i\rangle. \quad (6.30)$$

We can then use the known properties of the harmonic oscillator (see [105] or virtually any quantum mechanics textbook) to obtain selection rules for the different transitions. For the first term we make use of

$$\langle v_k^f | v_k^i \rangle = \delta_{f,i} \quad (6.31)$$

to realise that this term is non-zero only if $f = i$, i.e., it relates to Rayleigh scattering. For the second term we make use of the relations

$$\langle v_k^f | Q_k | v_k^i \rangle = \begin{cases} 0 & \text{for } v_k^f = v_k^i \\ a_{v_k} (v_k^i + 1)^{1/2} & \text{for } v_k^f = v_k^i + 1 \\ a_{v_k} (v_k^i)^{1/2} & \text{for } v_k^f = v_k^i - 1 \end{cases} \quad (6.32)$$

where $a_{v_k} = (\hbar/2\omega_k)^{1/2}$, to realise that for Raman scattering to occur for the vibrational mode k , we need to have $v_l^f = v_l^i$ for $l \neq k$, and $v_l^f = v_l^i + 1$ for $l = k$ (Stokes Raman scattering) or $v_l^f = v_l^i - 1$ for $l = k$ (anti-Stokes Raman scattering).

To sum up: In the approximation of electrical (only keeping terms linear in Q) and mechanical (using harmonic wavefunctions) harmonicity, only transitions in which only one vibrational quantum number changes are Raman active. In addition, just as in the classical case, the derivative $\alpha'_{\rho\sigma}$ of the polarisability with respect to the normal coordinate Q_k , has to be non-zero. When these requirements are fulfilled, the intensity from a scattering molecule is (Stokes scattering)

$$\alpha_{\rho\sigma} = a_{v_k} (v_k^i + 1)^{1/2} (\alpha'_{\rho\sigma})_k. \quad (6.33)$$

6.3.4 Scattering From a Collection of Molecules

To calculate the scattering intensity from a collection of N molecules, we also need to take into account that not all molecules are in their ground vibrational states. More specifically, the fraction of molecules in an initial state with quantum number v_k^l is given by the Boltzmann distribution

$$p_{v_k^l} = \frac{e^{-(v_k^l+1/2)\hbar\omega_k/k_B T}}{\sum_{v_k^m} e^{-(v_k^m+1/2)\hbar\omega_k/k_B T}}, \quad (6.34)$$

and to get the total intensity of a vibrational mode we need to calculate the sum over all allowed transitions

$$N \sum_{v_k^l=0}^{\infty} (v_k^l + 1) p_{v_k^l} = \frac{N}{1 - e^{-\hbar\omega_k/k_B T}}. \quad (6.35)$$

Combining the results from this section with equation (6.9) finally gives us the intensity of the k th vibrational mode from a collection of N molecules as

$$I_N = \frac{N \hbar \omega_s^4 \langle (\alpha')^2 \rangle}{32 \pi^2 \epsilon_0^2 c_0^4 \omega_k (1 - e^{-\hbar\omega_k/k_B T})} \mathcal{I}, \quad (6.36)$$

where $\omega_s = \omega_{\mathbf{E}} - \omega_k$ is the absolute frequency of the scattered light, the irradiance \mathcal{I} is defined by $\mathcal{I} = \frac{1}{2} \epsilon_0 c_0 E_0^2$, and $\langle (\alpha')^2 \rangle$ denotes an isotropic average over the derived polarisability tensor, i.e. we have assumed equal probabilities for the spatial orientation of the N molecules within the scattering volume.

6.4 The Role of Symmetries in Raman Scattering

In the measurements related to this thesis, we use our spectrometer in a back-scattering geometry, i.e. we measure light in the opposite direction of the incident laser beam. If the horizontal axis perpendicular to the incident beam is the x -axis and the vertical axis is the z -axis, we measure the two components of the derived polarisability tensor $\langle (\alpha'_{xx})^2 \rangle$ and $\langle (\alpha'_{zz})^2 \rangle$ and the intensities I_{xx} and I_{zz} are given by substituting these components for the general derived polarisability tensor in equation (6.36). As long as the polarisability tensor is symmetric, which it is according to equation (6.28), the components can be expressed in terms of the mean polarisability a

$$a = \frac{1}{3} (\alpha_{xx} + \alpha_{yy} + \alpha_{zz}), \quad (6.37)$$

and the anisotropy γ

$$\begin{aligned} \gamma^2 &= \frac{1}{2} (|\alpha_{xx} - \alpha_{yy}|^2 + |\alpha_{yy} - \alpha_{zz}|^2 + |\alpha_{zz} - \alpha_{xx}|^2) \\ &+ \frac{3}{4} (|\alpha_{xy} + \alpha_{yx}|^2 + |\alpha_{xz} + \alpha_{zx}|^2 + |\alpha_{yz} + \alpha_{zy}|^2) \end{aligned} \quad (6.38)$$

as

$$\langle (\alpha'_{xx})^2 \rangle = \frac{45a^2 + 4\gamma^2}{45} \quad (6.39)$$

and

$$\langle (\alpha'_{xz})^2 \rangle = \frac{\gamma^2}{15}. \quad (6.40)$$

The derivation of these formulae is rather lengthy, but can be found in e.g. [106]. Using equations (6.39) and (6.40) we can extract the *isotropic* and *anisotropic* parts of the spectrum:

$$I_a = I_{xx} - \frac{4}{3}I_{xz}, \quad (6.41)$$

$$I_\gamma = 15I_{xz}. \quad (6.42)$$

As will be explained on the following pages, a relates to vibrational modes which preserve the symmetry of the molecular- or intermolecular structure that the mode is related to. γ on the other hand, relates to modes which break this symmetry.

6.4.1 Molecular symmetries

All molecules belong to a specific symmetry group. A symmetry group consists of a number of symmetry operations such as rotations, reflections and inversion. When the operations in a molecule's symmetry group operate on the molecule, they will bring the molecule into a configuration identical to the one it was in before the operation. As an example, consider the water molecule, H_2O . Water belongs to the symmetry group C_{2v} which has four operations: the identity operation E , a rotation of $2\pi/2$ radians around (hence the 2 in C_{2v}) an axis C_2 that goes through the oxygen and right between the hydrogens, and two vertical (hence the v) planes of reflection; one through the plane of the molecule called σ , and one perpendicular to the plane of the molecule that goes through the oxygen called σ' . The symmetry elements C_2 , σ , and σ' are shown in figure 6.1. For the operations to form a mathematical group, they need to fulfil four properties

- Identity - one of the operations must be the identity operation
- Closure - it must be possible to write two consecutively applied operations as another operation. For the case of water we notice that the rotation C_2 followed by the reflection σ' is the same as the reflection σ' by itself, $\sigma' \cdot C_2 = \sigma'$. Note that the operations are applied from right to left.
- Associativity - the operations have to be associative, e.g. $(C_2\sigma)\sigma' = C_2(\sigma\sigma')$
- Inverse - each operation has to have an inverse that is also in the group. In the case of C_{2v} , all operations are their own inverses, e.g. $C_2 \cdot C_2 = E$

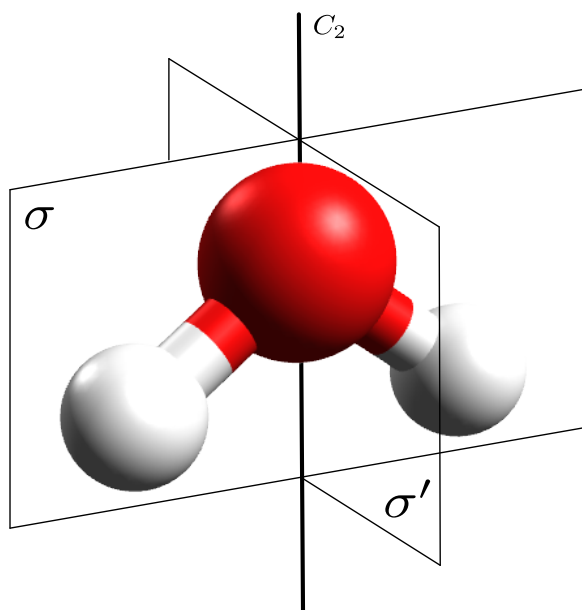


Figure 6.1: The symmetry elements of a water molecule

The operations can be represented by matrices. If we call the atoms in the water molecule H_1 , H_2 , and O we can for example write the reflection σ' which interchanges H_1 and H_2 as

$$\sigma' \begin{pmatrix} H_1 \\ H_2 \\ O \end{pmatrix} = \begin{pmatrix} 0 & 1 & 0 \\ 1 & 0 & 0 \\ 0 & 0 & 1 \end{pmatrix} \begin{pmatrix} H_1 \\ H_2 \\ O \end{pmatrix} = \begin{pmatrix} H_2 \\ H_1 \\ O \end{pmatrix}. \quad (6.43)$$

The representations are not unique, but can be decomposed, or reduced, into a set of unique *irreducible* representations by block diagonalising the matrix and taking the block matrices as the new representations. These irreducible representations can be shown to have the same group properties as the original reducible representation. Unfortunately, the irreducible representations are not unique either, but their *characters* are. A matrix' character is the same as the trace, or the sum of diagonal elements, of the matrix. All the characters of the different irreducible representations of the point group can then be presented in the form a *character table*. The character table for the point group C_{2v} is shown in table 6.1. The top row of the table starts with the name of the point group followed by the names of the symmetry elements of the point group. On the second row, the first column contains the name of the irreducible representation. The representations labeled A have character 1 under the principal rotation, in this case C_2 , while the representations labeled B have character -1. The characters under the identity operation E are also the dimension of that particular representation. For the case

C_{2v}	E	C_2	σ	σ'		
A_1	1	1	1	1	z	x^2, y^2, z^2
A_2	1	1	-1	-1	R_z	xy
B_1	1	-1	1	-1	x, R_y	xz
B_2	1	-1	-1	1	y, R_x	yz
$\Gamma_{x,y,z}$	3	-1	1	1		

Table 6.1: Character table for the point group of water, C_{2v}

of C_{2v} , all the irreducible representations are of order 1.

A_1 is called the *totally symmetric* representation and consists of all ones. To the right of the characters in the table are basis functions for the respective representations, i.e. functions which transform as that particular representation. To determine the representation of a particular basis function we first need to know that the z -axis is always defined to lie along the principal axis of rotation and the x -axis is in the plane of the molecule. We can then get the characters of a basis function, say x , by considering how arrows sitting on the atoms and pointing in the x -direction transforms under each symmetry operation. An arrow pointing in the x -direction will for example change sign under a C_2 -rotation, and also under a σ' -reflection. The characters of the bilinear functions x^2, xy , etc, can be obtained by multiplying the rows of the linear basis functions. The characters of xy for example, are given by $1 \times 1, -1 \times -1, 1 \times -1$, and -1×1 . A consequence of this, that will be of importance, is that the squares x^2, y^2, z^2 always transform as the totally symmetric representation. If we denote the symmetry species of x by Γ_x and the totally symmetric species by Γ_1 , this can be written as

$$\Gamma_x \times \Gamma_x = \Gamma_1. \quad (6.44)$$

6.4.2 Symmetry selection rule

Equation (6.27) enables determination of symmetry based selection rules. This becomes more evident if (6.27) is written as an integral over wave-functions

$$\alpha_{\rho\sigma} = \langle v^f | \hat{\alpha}_{\rho\sigma}(\{Q_k\}) | v^i \rangle = \int \phi_f(\mathbf{r}) \hat{\alpha}_{\rho\sigma}(\{Q_k\}) \phi_i(\mathbf{r}) d\mathbf{r}. \quad (6.45)$$

For a corresponding one-dimensional integral

$$\int_{-\infty}^{\infty} f(x)g(x)h(x)dx, \quad (6.46)$$

it is obvious that the integrand must be even for the integral not to vanish. Since the only symmetry operations in one dimension are reflection and inversion, both

bringing $x \rightarrow -x$, this is the same as saying that the integrand must contain the totally symmetric species, a statement that is true also for the three dimensional integrand in equation (6.45). Furthermore vibrational states with even quantum numbers only contain even powers of the vibrational normal coordinate Q_k , and since symmetry operations always transform Q_k into $\pm Q_k$, these states are always totally symmetric. Conversely, states with odd quantum number contain odd powers of Q_k and therefore always transform as the vibrational coordinate itself. If we assume that the initial state is the ground state and the final state is the first excited state we thus get

$$\Gamma_{\phi_f} \times \Gamma_{\phi_i} = \Gamma_{\phi_f}, \quad (6.47)$$

where Γ_{ϕ_f} then is the symmetry species of the vibration. Since only a product of two identical symmetry species gives the required totally symmetric species, $\hat{\alpha}_{\rho\sigma}(\{Q_k\})$ must also belong to the symmetry species of the vibration.

Regarding the transition polarisability tensor, it is essentially given by a product of two components $\langle f|\mu_\rho|r\rangle$ and $\langle r|\mu_\sigma|i\rangle$ of transition dipole moments. Since the transition dipole moment is a vector, its components transform as the basis functions x , y and z . The components of the transition polarisability tensor therefore transform as the bilinear products x^2 , xy , etc.

And now to the important conclusion of all this: The isotropic spectrum only involves the totally symmetric parts of the transition polarisability tensor (α_{xx} , α_{yy} , and α_{zz}), and can therefore only contain vibrational modes that preserve the symmetry of the molecule, i.e. vibrational modes that are totally symmetric. It *will* contain *all* symmetry preserving vibrations whose intensities are non-zero ($\alpha_{\rho\sigma} \neq 0$). The anisotropic spectrum, on the other hand, can contain vibrations of any symmetry, but modes that are *only* found in the anisotropic spectrum *cannot* be symmetry preserving.

It should be noted however, that these selection rules are based on some approximations (Born-Oppenheimer, non-interacting molecules, etc.) and theoretically forbidden modes are therefore sometimes seen experimentally.

6.5 Line Shapes in Vibrational Spectra

The previous sections on the theory of Raman scattering provided means to calculate vibrational frequencies and intensities from given properties of the material. As experimentalists we typically start from the other end, and the goal is to get as much information as possible out from a given spectrum or set of spectra. An important tool here is to fit the spectral lines, and then use the fitting parameters to get information about the material at hand. The spectral lines we need to fit are usually not lines at all, but instead broad bands, often tens or even hundreds of wavenumbers wide. To choose an appropriate fitting function, and to interpret

the information we get from the fitting parameters we need to understand the mechanisms behind the broadening of the lines. The mechanisms most important for this thesis and the appended papers will be discussed here.

In general, broadening of spectral lines are caused by fluctuations of the frequencies of the vibrating molecules, which in turn is caused by a fluctuating environment. In light of this, it is not surprising that liquids and other disordered materials usually have wider spectral lines than gases or crystalline solids. If the fluctuations are slow or static compared to the timescale of the experiment, the line shape simply reflects the distribution of frequencies in the material, which in turn provides information on the structure [107]. In the other limit of very fast fluctuations, the frequencies are averaged out, and the result is a spectral line that is narrower than the frequency distribution of the material.

6.5.1 Kubo's model

A classic model describing these features is the Kubo model [108]. In the Kubo model, the frequency fluctuations are described by an exponentially correlated Gaussian stochastic process, i.e. the momentary distribution of the (angular) frequency of a vibrational mode Ω is Gaussian:

$$p(\Omega) \propto e^{-\frac{(\Omega-\bar{\Omega})^2}{2\Delta^2}}, \quad (6.48)$$

with mean $\bar{\Omega}$ and variance Δ , and the frequency autocovariance function is exponential

$$C(t) = \langle \delta\Omega(t)\delta\Omega(0) \rangle = \Delta^2 e^{-t/\tau}, \quad (6.49)$$

where $\delta\Omega(t) = \Omega(t) - \bar{\Omega}$. The spectral intensity, i.e. the line shape is given by the power spectrum of the fluctuating induced dipole moment

$$I(\omega) \propto \int_{-\infty}^{\infty} dt e^{-i\omega t} \langle \mu_{\text{ind}}(t)\mu_{\text{ind}}(0) \rangle. \quad (6.50)$$

For a non-fluctuating static frequency Ω , the induced dipole moment can be written as $\mu_{\text{ind}}(t) = \mu(0)e^{-i\Omega t}$ and the power spectrum is just a δ -function, $I(\omega) \propto \delta(\omega - \Omega)$. The total intensity of the vibrational mode in equation (6.9) is then given by the integral over all frequencies $I_{\text{tot}} = \int_{-\infty}^{\infty} d\omega I(\omega)$.

For a time dependent frequency $\Omega(t)$ on the other hand, the exponential $i\Omega t$ has to be replaced by an integral

$$\mu(t) = \mu(0)e^{-i\int_0^t d\tau\Omega(\tau)} = \mu(0)e^{-i\bar{\Omega}t - i\int_0^t d\tau\delta\Omega(\tau)}, \quad (6.51)$$

and the autocovariance function becomes

$$\langle \mu(t)\mu(0) \rangle = |\mu(0)|^2 e^{-i\bar{\Omega}t} F(t), \quad (6.52)$$

with

$$\begin{aligned}
 F(t) &= \langle e^{-i \int_0^t d\tau \delta\Omega(\tau)} \rangle \\
 &= \text{[cumulant expansion, change of variables, etc.]} \\
 &= e^{-\int_0^t d\tau (t-\tau) C(\tau)} \\
 &= e^{-g(t)}.
 \end{aligned} \tag{6.53}$$

The intensity thus becomes

$$I(\omega) \propto \int_{-\infty}^{\infty} dt e^{-i(\omega - \bar{\Omega})t} e^{-g(t)}. \tag{6.54}$$

For an exponential time decay $g(t)$ evaluates to

$$g(t) = \Delta^2 \tau t + \Delta^2 \tau^2 (e^{-t/\tau} - 1), \tag{6.55}$$

and for large times t , the first term $\Delta^2 \tau t$ will dominate and if $\Delta^2 \tau t \gg 1$ then $e^{-g(t)}$ will be small and wont contribute to the integral. The times that do contribute to the integral are thus the times where

$$\Delta^2 \tau t \lesssim 1 \Leftrightarrow \Delta t \lesssim \frac{1}{\Delta \tau}. \tag{6.56}$$

For $\Delta \tau \gg 1$ we get $\Delta t \ll 1$ in the contributing time domain and thus $t/\tau \ll 1$, and we can expand the exponential in $g(t)$ to obtain

$$g(t) \approx \Delta \tau t' + \Delta^2 \tau^2 \left(-t'/\Delta \tau + \frac{1}{2} (t'/\Delta \tau)^2 \right) = \frac{\Delta^2 t'^2}{2}, \tag{6.57}$$

which leads to a Gaussian line shape with width Δ :

$$I_G(\omega) \propto e^{-\frac{(\omega - \bar{\Omega})^2}{2\Delta^2}}. \tag{6.58}$$

For $\Delta \tau \ll 1$, on the other hand, we get $t/\tau \gg 1$ and the first term of $g(t)$ dominates

$$g(t) \approx \Delta^2 \tau t. \tag{6.59}$$

We then get a Lorentzian line shape with full width at half maximum (FWHM) $\Delta^2 \tau$

$$I_L(\omega) \propto \frac{\Delta^2 \tau}{(\omega - \bar{\Omega})^2 + (\Delta^2 \tau)^2}. \tag{6.60}$$

6.5.2 A Generalised Kubo Model

In Kubo's original theory, the frequency is only affected by one process with one single time constant τ . In real systems there are typically more than one process influencing the frequency, and depending on the system at hand, the different time scales might be either separated by orders of magnitude or quite close to each other. In liquids, the latter is often the case [107]. Either way, the simplest extension of the Kubo model is to write the autocovariance function as a sum of two exponentials with different relaxation times τ_1 and τ_2 , and different strength Δ_1 and Δ_2 [107]:

$$C(t) = \langle \delta\Omega(t)\delta\Omega(0) \rangle = \Delta_1^2 e^{-t/\tau_1} + \Delta_2^2 e^{-t/\tau_2}. \quad (6.61)$$

In this model $g(t)$ becomes

$$g(t) = \Delta_1^2 \tau_1 t + \Delta_1^2 \tau_1^2 (e^{-t/\tau_1} - 1) + \Delta_2^2 \tau_2 t + \Delta_2^2 \tau_2^2 (e^{-t/\tau_2} - 1). \quad (6.62)$$

If one time scale, say τ_1 is large enough, and the other time scale small enough, we can approximate $g(t)$

$$g(t) = \frac{\Delta_1^2 t^2}{2} + \Delta_2^2 \tau_2 t. \quad (6.63)$$

$F(t)$ can then be written as product of two functions, one giving a Gaussian line shape and one giving a Lorentzian line shape. In the frequency domain this becomes a convolution of the two line shapes

$$I(\omega) \propto \int_{-\infty}^{\infty} d\omega^* I_G(\omega^*) I_L(\omega - \omega^*). \quad (6.64)$$

The convolution of the Gaussian and the Lorentzian line shapes is usually referred to as the Voigt profile. Skinner [107] showed that if the two amplitudes Δ_1 and Δ_2 are equal, which is a good approximation in room temperature liquids, then the Voigt approximation is valid as long as the two time scales fulfil $\tau_1 \lesssim 6\tau_2$.

The exponential covariance function implies, according to Doob's theorem [92, 109], that the equation of motion of the fluctuating frequency is a Langevin equation familiar from the theory of Brownian motion

$$\frac{d\Omega(t)}{dt} = -\xi\Omega(t) + R(t), \quad (6.65)$$

where ξ is a damping coefficient and $R(t)$ is a random (generalised) force with zero mean ($\langle R(t) \rangle = 0$) and infinitely short time correlation ($\langle R(t)R(0) \rangle \propto \delta(t)$). Assuming an infinitely short correlation time is the same as saying that the process is Markovian or that it has no memory. The Markovian property of this process, and hence the exponentiality of the frequency autocovariance function has been questioned [110], but is a good enough approximation in most cases.

6.6 The Dilor Spectrometer

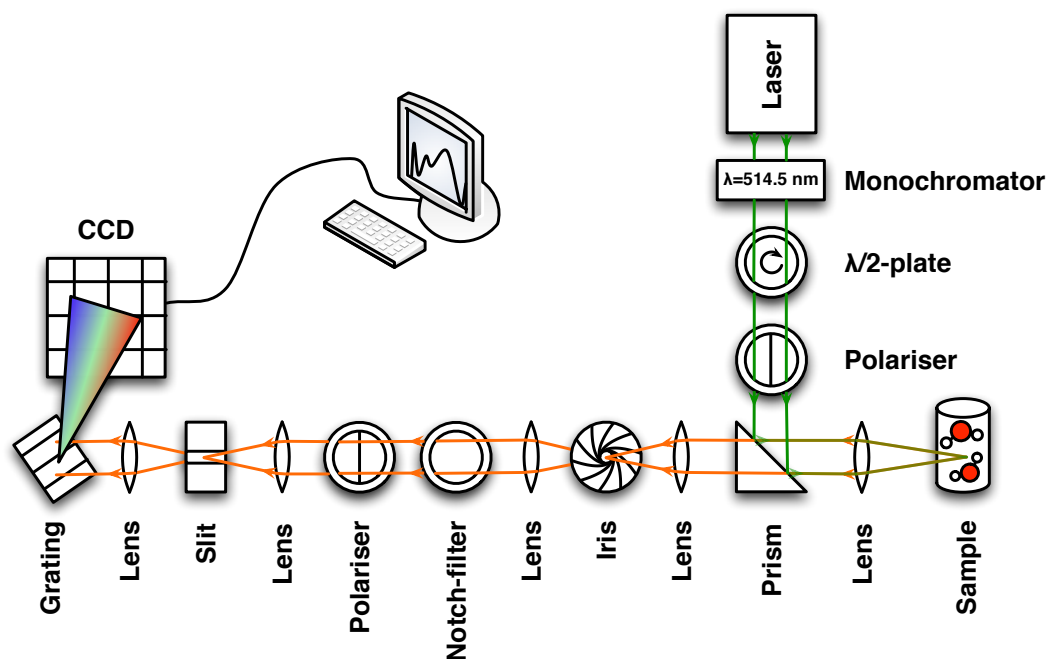


Figure 6.2: Schematics of the Dilor spectrometer

The Raman spectrometer used for the experiments presented here is shown schematically in figure 6.2. The laser was an argon/krypton ion laser from which we have used the 514.5 nm line to excite vibrations in our liquids. The laser first passes through a monochromator to make sure the exciting beam only contains 514.5 nm light. The combination of a $\lambda/2$ -plate and a polariser is then used to choose between horizontal and vertical polarisation of the incident radiation. A prism is used to guide the light through a lens focused on a μm sized volume inside the liquid sample, and some of the light scattered from this volume goes back through the same lens and through the prism. Another lens focuses the beam on an iris, cutting away unwanted light not coming from the sample. After the beam has been parallelised by yet another lens it goes through a notch filter which removes the Rayleigh scattered light of 514.4 nm. Another polariser, or analyser, is then used to determine the polarisation of the measured spectrum. The beam then passes a slit that can be adjusted to optimise resolution, and then, after being made parallel again, finally hits a 300 line/mm grating which essentially splits the light into its frequency components that are then recorded by a CCD-camera.

The samples were either placed in a liquid nitrogen cooled cryostat for low temperature measurements, or a furnace for experiments above 300 K.

7

Monte Carlo and EPSR Simulations

To understand a liquids structure in detail it is usually necessary to complement experiments with computational methods. The options at hand are basically classical molecular dynamics simulations (MD) or Monte Carlo simulations (MC) or a variety of quantum mechanical ab initio methods [11, 111]. Quantum mechanical methods are more exact, but usually not fast enough to calculate structures of more than a few molecules. Out of the classical methods I have chosen the MC approach, together with the closely related EPSR (empirical potential structure refinement) technique [13]. The latter uses neutron or X-ray diffraction data to refine the intermolecular interactions, to improve the agreement between simulated and experimental data. The simulations essentially produce a set of equilibrium configurations of, in this case, 500-2100 molecules. We can then average over the set of simulated configurations to obtain measures of the structure, such as pair correlation functions, $g(r)$, cluster size distributions or H-bonding angles. The results can then be compared with and analysed together with experimental results to give a better understanding of the liquid structure. Here I will focus on the inner workings of the Metropolis Monte Carlo algorithm, and the EPSR technique, while the results of the simulations are presented in the appended papers. For a more complete text on molecular simulations than the one presented here, see e.g. [111].

7.1 The Metropolis Algorithm

The task of the Monte Carlo simulation is to sample the Boltzmann distribution related the potential energy function $V(\mathbf{r}^N)$ of the system.

$$p(\mathbf{r}^N) = \frac{e^{-\frac{V(\mathbf{r}^N)}{k_B T}}}{Z}, \quad (7.1)$$

Z being the so called configuration integral $Z = \int e^{-\frac{V(\mathbf{r}^N)}{k_B T}} d\mathbf{r}^N$ that is there to normalise the distribution. The specific algorithm most commonly used, also in this case, is the Metropolis algorithm which dates back to 1953 [112] and is a specific case of a Markov chain Monte Carlo approach. It is called Monte Carlo, as in the gambling resort, because it relies on random numbers and the Markov chain property means that the algorithm has a very short memory as will be described shortly. The Metropolis algorithm proceeds in four simple steps:

1. Choose a starting point with positive probability $p(\mathbf{r}^N)$. As long as there are no hard core interactions, all configurations \mathbf{r}^N have non-zero probability, so the starting configuration can be completely random.
2. Draw a new proposed configuration, $\mathbf{r}^N(*)$, from a jumping distribution $J(\mathbf{r}^N(*)|\mathbf{r}^N(t-1))$.
3. Calculate the ratio of probabilities for the new and the old state

$$r = \frac{p(\mathbf{r}^N(*))}{p(\mathbf{r}^N(t-1))} = e^{-\frac{V(\mathbf{r}^N(*)) - V(\mathbf{r}^N(t-1))}{k_B T}}. \quad (7.2)$$

4. Choose the new state according to

$$\mathbf{r}^N(t) = \begin{cases} \mathbf{r}^N(*) & \text{with probability } \min(r, 1) \\ \mathbf{r}^N(t-1) & \text{otherwise} \end{cases} \quad (7.3)$$

A few crucial points about the jumping distribution must also be mentioned. Typically one moves one atom or molecule at a time, keeping the rest of the coordinates unchanged. The jumping distribution is also where the Markov property comes in - the proposed new coordinates, $\mathbf{r}^N(*)$, only depend on the coordinates at the nearest previous time $t-1$ but are independent on the earlier history of the simulation. In the simple Metropolis algorithm, the jumping distribution must be symmetric, i.e. it must satisfy $J(\mathbf{r}^N(*)|\mathbf{r}^N(t-1)) = J(\mathbf{r}^N(t-1)|\mathbf{r}^N(*))$. This is typically achieved by simply translating the atom or molecule a uniformly distributed distance centred at the current position, and rotating the molecule a uniformly distributed angle, and also randomly choosing which one, translation or rotation, to do first.

Another crucial point is that it is sufficient to know the relative probabilities of two different states, i.e. we do not have to know the configuration integral Z to sample from the distribution. This is essential since the only reasonable way to get an estimate of Z is through an MC, or MD simulation!

7.2 Intermolecular Interactions - OPLS-AA

The potential function, or force field, $V(\mathbf{r}^N)$ is the input to the simulation, and also what determines the outcome. In the work presented I have used the OPLS-AA (Optimised Potentials for Liquid Simulations - All Atoms) potential model as a starting point for the intermolecular interactions. In Paper II, the potential is then modified according to the EPSR algorithm described below.

The OPLS force field, as the name suggests, is a potential model that have been optimised to reproduce a number of properties of organic materials, e.g. heat of vaporisation, heat capacities, isothermal compressibilities, and densities [113]. The functional form of the OPLS potential is that of a pairwise additive Lennard-Jones potential plus Coulomb forces, so that the potential energy of two interacting molecules i and j is

$$v_{ij}(\mathbf{r}) = \sum_k^{\text{on } i} \sum_l^{\text{on } j} \frac{q_k q_l}{4\pi\epsilon_0 r_{kl}} + 4\epsilon_{kl} \left[\left(\frac{\sigma_{kl}}{r_{kl}} \right)^{12} - \left(\frac{\sigma_{kl}}{r_{kl}} \right)^6 \right], \quad (7.4)$$

where ϵ_0 is the vacuum permittivity, q_k is the (partial) charge on atom k and r_{kl} is the distance between atoms k and l . The total potential energy is given by the sum over all molecules

$$V(\mathbf{r}^N) = \sum_i \sum_{j>i} v_{ij}(\mathbf{r}). \quad (7.5)$$

7.3 Intramolecular interactions

Internally in the molecules, the forces between atoms are governed by harmonic potentials. The inputs are the bond lengths, bond angles and the total intramolecular potential energy is then given by

$$V_{\text{intra}} = \frac{C}{2} \sum_i \sum_{k \neq l} \frac{(r_{kl} - d_{kl})^2}{w_{kl}^2}. \quad (7.6)$$

where a good value of $C/2$ is determined from matching the high Q part of the simulated structure factor with measured diffraction data. For the case of 1-propanol, a value of $35 \text{J}\text{\AA}^{-1} (\text{atomic mass units})^{-1/2}$ gave the best agreement. The denominator is given by

$$w_{kl}^2 = \frac{d_{kl}}{\sqrt{\mu_{kl}}} = d_{kl} \sqrt{\frac{M_k + M_l}{M_k M_l}}, \quad (7.7)$$

with d_{kl} being the equilibrium distance between atom k and l , and M_k is the mass of atom k .

7.4 The EPSR technique

In an EPSR simulation [13, 16, 114], a reference potential, such as the OPLS-AA forcefield described above is used as a starting point. It is then modified, by adding an empirical potential, U^{EP} , in order to improve the agreement between simulated and measured structure factors. The empirical potential

$$U^{\text{EP}}(r) = k_B T \sum_i C_i p_{n_i}(r, \sigma_r), \quad (7.8)$$

is a weighted sum of power exponential functions,

$$p_{n_i}(r, \sigma) = \frac{1}{4\pi\rho\sigma^3(n_i + 2)!} \left(\frac{r}{\sigma}\right)^{n_i} e^{-r/\sigma}, \quad (7.9)$$

where $n_i = r_i/\sigma - 3$ is chosen to give the empirical potential a suitable range. The advantage of using this form for the empirical potential is that it has an analytical Fourier transform

$$\hat{U}^{\text{EP}}(Q) = k_B T \sum_i C_i \hat{p}_{n_i}(Q, \sigma_Q), \quad (7.10)$$

where

$$\hat{p}_{n_i}(Q, \sigma_Q) = \frac{1}{(n+2)(1+Q^2\sigma^2)^{(n+4)/2}} \left(2 \cos(n\alpha) + \frac{1-Q^2\sigma^2}{Q\sigma} \sin(n\alpha) \right), \quad (7.11)$$

and $\alpha = \arctan(Q\sigma)$. The weights, C_i , are then determined from fitting the potential in Q-space to the difference between the simulated and the measured structure factors. As the simulation proceeds the weights, $C_{i,m}$, calculated at step m , should become smaller and smaller, and the empirical potential should converge to a final form. The simulation then proceeds into the production phase, where desired properties, such as partial distribution functions, bonding angles, cluster sizes, etc. are calculated and averaged over the production run.

The most common alternative to using EPSR in analysing diffraction data is the Reverse Monte Carlo (RMC) approach [115], which uses the difference between measured and simulated structure factors directly, rather than potential energy, as acceptance criterion for the trial moves in the Metropolis algorithm described in section 7.1. While the RMC technique usually gives good agreement between simulated and measured structure factors, the resulting structures are often implausible from an energetic point of view. The results of using EPSR together with neutron diffraction data from 1-propanol are presented in Paper II.

8

Summary of Appended Papers

Paper I. A statistical model of hydrogen bond networks in liquid alcohols

To better understand and interpret experimental results regarding hydrogen bonded materials, an accurate quantitative model is needed, that captures the structural properties of the H-bonded clusters. In Paper I we derive a statistical model of H-bonded clusters in liquid alcohols that extends previous models by allowing the first H-bond connected to a given hydroxyl group's oxygen to have a different bonding probability compared to the second one. The size distribution of the tree-like clusters thus obtained, as well as its mean and variance, are calculated in terms of two bonding probabilities, and benchmarked against Monte Carlo simulation data of six different mono and poly alcohols. The average size of the H-bonded clusters range from 1.4 for propylene glycol mono-methyl ether, to 5.9 for methanol. The fraction of “leaves”, “roots”, and internal nodes are also calculated.

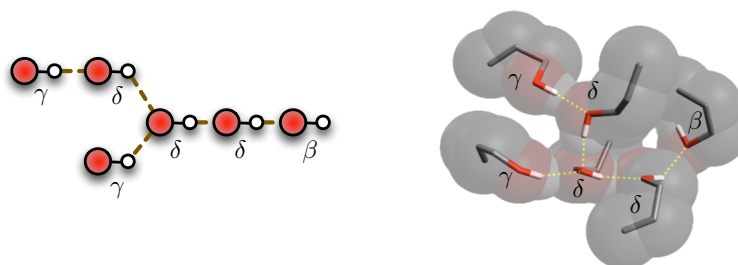


Figure 8.1: An example cluster as described by the statistical model in Paper I. The labels β , γ , and δ denote root, leaf, and internal nodes of the cluster.

Paper II. Temperature dependence of the hydrogen bond structure of liquid 1-propanol by neutron diffraction and EPSR Simulations

The size distribution, shape and topology of H-bonded clusters in mono alcohols are still debated. In Paper II we present the results of a neutron diffraction experiment performed on 1-propanol. We use the EPSR technique, together with the model in Paper I, to analyse the diffraction data. The focus is on the temperature dependence of the properties of the H-bonded clusters. To characterise the clusters, we calculate cluster size distributions, the principal components of the gyration tensor, as well as H-bond angles within the clusters. The average cluster size increases from 3.3 at 293 K to 6.0 at 155 K. The shapes of the clusters, as determined from the principal components of the gyration tensor, is ellipsoidal, with three distinct semi-axis. The H-bonding angles show only a weak temperature dependence, with slightly more straight H-bonds at lower temperatures.

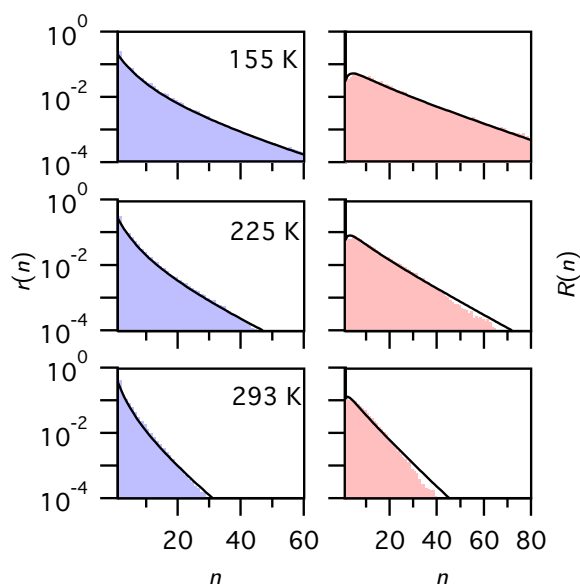


Figure 8.2: The temperature dependent cluster size distributions of 1-propanol obtained from neutron diffraction and EPSR simulations.

Paper III. On the use of vibrational spectroscopy to determine the temperature dependent hydrogen bond structure in alcohols

Vibrational spectroscopy (IR and Raman) has often been used to study the structure of water, alcohols and other H-bonded systems. The degree of H-bonding has a strong effect on the OH-stretch frequency in the wavenumber region $3000\text{--}4000\text{ cm}^{-1}$ and can thus be used to characterise the H-bonding situation in the material under investigation. While most IR and Raman studies discuss the structure on a qualitative level, in Paper III we show that the structure of alcohols, in terms of the statistical model of Paper I, can be quantitatively related to the OH-stretch band. The procedure is far from trivial, however, and the results obtained depend heavily on the exact assumptions made about H-bonding species and their vibrational frequencies and relative scattering cross section (here computed by DFT methods). Hence, an important conclusion is that, while the results are in reasonable agreement with results from computer simulations and neutron diffraction, they are not conclusive on their own, and should always be verified by other techniques.

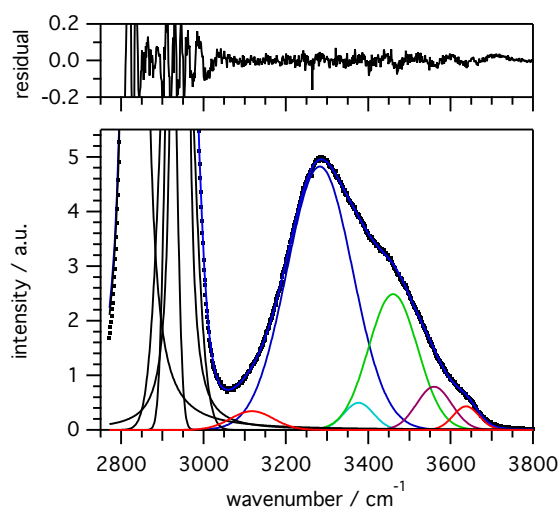


Figure 8.3: The wide OH-stretch band of methanol is fitted by 6 bands corresponding to different H-bonding configurations.

Paper IV. Queueing theory unravels the transient H-bonded chain dynamics in liquid alcohols

The dynamics of the H-bonded clusters in mono alcohols has previously been described by the transient chain model, wherein H-bonded chains grow and shrink as an effect of monomers joining and leaving the chain cluster at the ends. This type of dynamics is suggested to result in the so called Debye peak seen in dielectric spectra of mono alcohols. The master equation describing this type of dynamics is identical to the one describing a queue where customers join with a fixed average rate λ , and leave with a fixed average rate μ . This is referred to as an M/M/1 queue in the queueing theory literature, and was studied extensively during the mid 20th century. In Paper IV we use the results from queueing theory, especially the size autocorrelation function, to calculate the dielectric relaxation spectrum of the cluster dipole moments. The resulting function is fitted to dielectric spectra from literature to obtain H-bonding probabilities and cluster size distributions of 1-propanol. The obtained average cluster sizes range from 1 close to the boiling point, to about 8 just below the melting temperature, in good agreement with our neutron diffraction results.

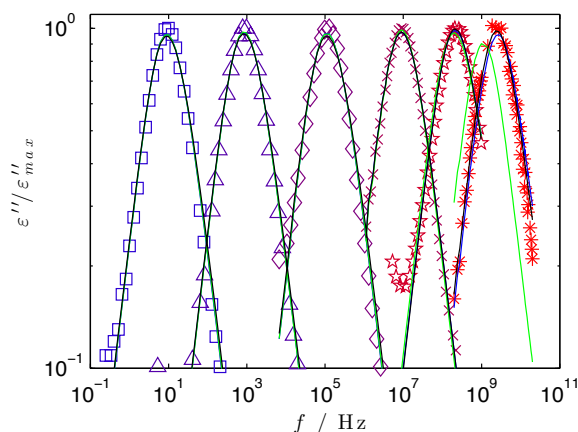


Figure 8.4: The temperature dependent dielectric Debye peak of 1-propanol fitted by fitting functions based on results from queueing theory. Data taken from reference [63].

Paper V. High-frequency properties of liquid 1-propanol studied by neutron scattering, near-infrared, and dielectric spectroscopy

Dynamics in alcohols has previously been studied by a number of techniques, such as dielectric spectroscopy, rheology, and NMR. The relationship between the different relaxation time scales found, and their relation to the H-bonded clusters are still not fully understood. In Paper V we use quasi elastic neutron scattering and the neutron spin echo technique to investigate the length scale dependence (in terms of the momentum transfer dependence) of the relaxation times in 1-propanol. The relaxation times at length scales corresponding to intermolecular distances is shown to correspond to the relaxation times obtained from temperature dependent viscosity and shear modulus measurements, and is faster but shows a similar temperature dependence as the dielectric α relaxation. At length scales corresponding to the pre-peak of the static structure factor, which has been suggested to correspond to distances between the H-bonded clusters, the relaxation time is longer and is in good agreement with the relaxation of OH-groups within clusters as measure by NMR. This relaxation time has been suggested to correspond to the average time an OH-group spends in an H-bonded cluster, and the ratio between this relaxation time and the α -relaxation time should be equal to the average cluster size.

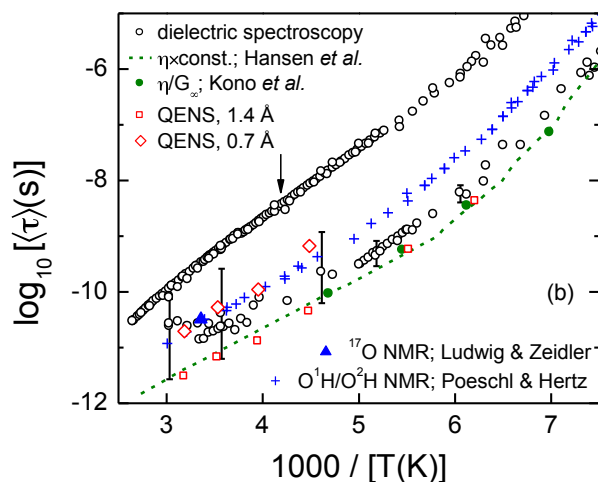


Figure 8.5: Comparison of relaxation times obtained by different techniques. The relaxation times obtained from neutron scattering are in good agreement with those obtained by mechanical relaxation [116] and NMR respectively. The Debye relaxation seen in dielectric measurement is not accessible by neutron scattering

Bibliography

- [1] H. E. STANLEY, P. KUMAR, L. XU, Z. YAN, M. G. MAZZA, S. V. BULDYREV, S. H. CHEN, and F. MALLAMACE, *Physica A* **386**, 729 (2007).
- [2] R. POLITI and D. HARRIES, *Chem. Commun.* **46**, 6449 (2010).
- [3] R. GILMAN-POLITI and D. HARRIES, *J. Chem. Theory. Comput.* **7**, 3816 (2011).
- [4] F. DAVIS, *Adv. Drug Deliver Rev.* **54**, 457 (2002).
- [5] T. TAKAMUKU, H. MARUYAMA, K. WATANABE, and T. YAMAGUCHI, *J. Sol. Chem.* **33**, 641 (2004).
- [6] H. JANSSON and J. SWENSON, *J. Chem. Phys.* **134**, 104504 (2011).
- [7] J. MATTSSON, R. BERGMAN, P. JACOBSSON, and L. BÖRJESSON, *Phys. Rev. B* **79**, 174205 (2009).
- [8] C. M. ROLAND, R. CASALINI, R. BERGMAN, and J. MATTSSON, *Phys. Rev. B* **77**, 012201 (2008).
- [9] C. GAINARU, R. MEIER, S. SCHILDMANN, C. LEDERLE, W. HILLER, E. RÖSSLER, and R. BÖHMER, *Phys. Rev. Lett.* **105**, 258303 (2010).
- [10] D. F. EVANS and H. WENNERSTRÖM, *The Colloidal Domain*, Wiley-VCH, 2 edition, 1994.
- [11] J. P. HANSEN and I. R. MCDONALD, *Theory of Simple Liquids*, Academic Press, Amsterdam, 3 edition, 2006.
- [12] L. OJAMÄE, *The Water Molecule in Gaseous, Liquid and Solid Surroundings*, PhD thesis, Uppsala University, 1993.
- [13] A. SOPER, *Chem. Phys.* **202**, 295 (1996).
- [14] P. SILLRÉN, J. SWENSON, J. MATTSSON, D. BOWRON, and A. MATIC, *J. Chem. Phys.* **138**, 214501 (2013).

- [15] K. OHNO, T. SHIMOAKA, N. AKAI, and Y. KATSUMOTO, *J. Phys. Chem. A* **112**, 7342 (2008).
- [16] T. YAMAGUCHI, K. HIDAKA, and A. SOPER, *Mol. Phys.* **96**, 1159 (1999).
- [17] D. BOWRON, J. FINNEY, and A. SOPER, *Mol. Phys.* **93**, 249 (1998).
- [18] P. SILLRÉN, J. BIELECKI, J. MATTSSON, L. BÖRJESSON, and A. MATIC, *J. Chem. Phys.* **136**, 094514 (2012).
- [19] F. PALOMBO, P. SASSI, M. PAOLANTONI, and A. MORRESI, *J. Phys. Chem. B* **110**, 18017 (2006).
- [20] M. PAOLANTONI, P. SASSI, A. MORRESI, and R. CATALIOTTI, *Chem. Phys.* **310**, 169 (2005).
- [21] M. PAOLANTONI, P. SASSI, A. MORRESI, and R. CATALIOTTI, *J. Raman Spectroscopy* **37**, 528 (2006).
- [22] I. AKIYAMA, M. OGAWA, K. TAKASE, T. TAKAMUKU, T. YAMAGUCHI, and N. OHTORI, *J. Sol. Chem.* **33** (2004).
- [23] A. MIKUSINSKA-PLANNER, *Acta Cryst. A* **33**, 433 (1977).
- [24] E. TSUCHIDA, Y. KANADA, and M. TSUKADA, *Chem. Phys. Lett.* **311**, 236 (1999).
- [25] T. KOSZTOLANYI, I. BAKÓ, and G. PÁLINKÁS, *J. Chem. Phys.* **118**, 4546 (2003).
- [26] K. VAHVASELKA, R. SERIMAA, and M. TORKKELI, *J. Appl. Crystallography* **28**, 189 (1995).
- [27] H. GRAENER, T. Q. YE, and A. LAUBEREAU, *J. Chem. Phys.* **90**, 3413 (1988).
- [28] H. GRAENER, T. Q. YE, and A. LAUBEREAU, *J. Chem. Phys.* **91**, 1043 (1989).
- [29] L. SAIZ, J. A. PADRÓ, and E. GUÀRDIA, *J. Phys. Chem. B* **101**, 78 (1997).
- [30] J. A. PADRÓ, L. SAIZ, and E. GUÀRDIA, *J. Molec. Struct.* **416**, 243 (1997).
- [31] M. HAUGHNEY, M. FERRARIO, and I. McDONALD, *J. Phys. Chem.* **91**, 4934 (1987).

- [32] I. SVISHCHEV and P. KUSALIK, *J. Chem. Phys.* **100**, 5165 (1994).
- [33] E. BIANCHI, R. BLAAK, and C. N. LIKOS, *Phys. Chem. Chem. Phys.* **13**, 6397 (2011).
- [34] K. LIN, X. ZHOU, Y. LUO, and S. LIU, *J. Phys. Chem. B* **114**, 3567 (2010).
- [35] G. W. STEWART and R. M. MORROW, *Phys. Rev.* **30**, 232 (1927).
- [36] A. VRHOVSEK, O. GEREKEN, A. JAMNIK, and L. PUSZTAI, *J. Phys. Chem. B* **115**, 13473 (2011).
- [37] J. TOWEY, A. SOPER, and L. DOUGAN, *Phys. Chem. Chem. Phys.* **13**, 9397 (2011).
- [38] R. LUDWIG, *Chem. Phys. Chem.* **6**, 1369 (2005).
- [39] L. ROOT and F. STILLINGER, *J. Chem. Phys.* **90**, 1200 (1989).
- [40] I. BAKÓ, P. JEDLOVSZKY, and G. PÁLINKÁS, *J. Molec. Liq.* **87**, 243 (2000).
- [41] M. TOMSIČ, A. JAMNIK, G. FRITZ-POPOVSKI, O. GLATTER, and L. VLČEK, *J. Phys. Chem. B* **111**, 1738 (2007).
- [42] V. CRUPI, F. LONGO, D. MAJOLINO, and V. VENUTI, *J. Molec. Struct.* **790**, 141 (2006).
- [43] A. SAHOO, S. SARKAR, V. BHAGAT, and R. N. JOARDER, *J. Phys. Chem. A* **113**, 5160 (2009).
- [44] G. WALRAFEN, *J. Chem. Phys.* **47**, 114 (1967).
- [45] G. D'ARRIGO, G. MAISANO, F. MALLAMACE, P. MIGLIARDO, and F. WANDERLINGH, *J. Chem. Phys.* **75**, 4264 (1981).
- [46] D. E. HARE and C. M. SORESENSEN, *J. Chem. Phys.* **93**, 25 (1990).
- [47] J. L. GREEN, A. R. LACEY, and M. G. SCEATS, *J. Chem. Phys.* **90**, 3958 (1986).
- [48] J. BRUBACH, A. MERMET, A. FILABOZZI, A. GERSCHEL, and P. ROY, *J. Chem. Phys.* **122**, 184509 (2005).
- [49] F. MALLAMACE, M. BROCCIO, C. CORSARO, A. FARAONE, D. MAJOLINO, V. VENUTI, L. LIU, C. MOU, and S. CHEN, *PNAS* **104**, 424 (2007).

- [50] L. XU, F. MALLAMACE, Z. YAN, F. W. STARR, S. V. BULDYREV, and H. E. STANLEY, *Nature Physics* **5**, 565 (2009).
- [51] B. M. AUER and J. L. SKINNER, *J. Chem. Phys.* **128**, 224511 (2008).
- [52] R. JIANG and E. L. SIBERT, III, *J. Phys. Chem. A* **113**, 7275 (2009).
- [53] S. MIZUSHIMA, *Bulletin of the Chemical Society of Japan* **1**, 163 (1926).
- [54] M. PREUSS, C. GAINARU, T. HECKSHER, S. BAUER, J. C. DYRE, R. RICHERT, and R. BÖHMER, *J. Chem. Phys.* **137**, 144502 (2012).
- [55] C. GAINARU, S. KASTNER, F. MAYR, P. LUNKENHEIMER, S. SCHILDMANN, H. J. WEBER, W. HILLER, A. LOIDL, and R. BÖHMER, *Phys. Rev. Lett* **107**, 118304 (2011).
- [56] Y. YOMOGIDA, Y. SATO, R. NOZAKI, T. MISHINA, and J. NAKAHARA, *J. Molec. Liq.* **154**, 31 (2010).
- [57] T. E. GORESRY and R. BÖHMER, *J. Chem. Phys.* **128**, 154520 (2008).
- [58] L. WANG and R. RICHERT, *J. Phys. Chem. B* **109**, 8767 (2005).
- [59] L. M. WANG and R. RICHERT, *J. Chem. Phys.* **121**, 11170 (2004).
- [60] U. KAATZE, R. BEHRENDTS, and R. POTTEL, *J. Non-Crystalline Solids* **305**, 19 (2002).
- [61] O. KALINOVSKAYA, J. VIJ, and G. JOHARI, *J. Phys. Chem. A* **105**, 5061 (2001).
- [62] G. JOHARI, O. KALINOVSKAYA, and J. VIJ, *J. Chem. Phys.* **114**, 4634 (2001).
- [63] F. STICKEL, E. W. FISCHER, and R. RICHERT, *J. Chem. Phys.* **104**, 2043 (1996).
- [64] C. HANSEN, F. STICKEL, T. BERGER, R. RICHERT, and E. FISCHER, *J. Chem. Phys.* **107**, 1086 (1997).
- [65] P. BORDEWIJK, F. GRANSCH, and C. BÖTTCHER, *Transactions of the Faraday Society* **66**, 293 (1970).
- [66] D. W. DAVIDSON and R. H. COLE, *J. Chem. Phys.* **19**, 1484 (1951).
- [67] G. OSTER and J. G. KIRKWOOD, *J. Chem. Phys.* **11**, 175 (1943).
- [68] M. PÖSCHL and H. G. HERTZ, *J. Phys. Chem.* **98**, 8195 (1994).

- [69] B. JAKOBSEN, C. MAGGI, T. CHRISTENSEN, and J. C. DYRE, *J. Chem. Phys.* **129**, 184502 (2008).
- [70] R. JONES, *Soft Condensed Matter*, Oxford Master Series in Physics, Oxford University Press, Oxford, 2002.
- [71] B. JAKOBSEN, T. HECKSHER, T. CHRISTENSEN, N. B. OLSEN, J. C. DYRE, and K. NISS, *J Chem Phys* **136**, 081102 (2012).
- [72] P. DEBYE, *Verh. dt. phys. Ges.* **15**, 777 (1913).
- [73] P. DEBYE, *Polar Molecules (Chemical Catalog, New York, 1929)* .
- [74] Y. HIEJIMA, Y. KAJIHARA, H. KOHNO, and M. YAO, *J. Phys.: Condens. Matter* **13**, 10307 (2001).
- [75] F. DOLEZALEK, *Z. Phys. Chem.* **64**, 727 (1908).
- [76] A. APELBLAT, *J. Molec. Liq.* **128**, 1 (2006).
- [77] E. MULLER and K. GUBBINS, *Ind. Eng. Chem. Res.* **40**, 2193 (2001).
- [78] M. S. WERTHEIM, *J. Stat. Phys.* **35**, 19 (1984).
- [79] M. S. WERTHEIM, *J. Stat. Phys.* **35**, 35 (1984).
- [80] M. S. WERTHEIM, *J. Stat. Phys.* **42**, 459 (1986).
- [81] M. S. WERTHEIM, *J. Stat. Phys.* **42**, 477 (1986).
- [82] W. G. CHAPMAN, K. E. GUBBINS, G. JACKSON, and M. RADOSZ, *Fluid Phase Equilibria* **52**, 31 (1989).
- [83] W. G. CHAPMAN, K. E. GUBBINS, G. JACKSON, and M. RADOSZ, *Ind. Eng. Chem. Res.* **29**, 1709 (1990).
- [84] S. P. TAN, H. ADIDHARMA, and M. RADOSZ, *Ind. Eng. Chem. Res.* **47**, 8063 (2008).
- [85] C. MCCABE and A. GALINDO, SAFT associating fluids and fluid mixtures, in *Applied Thermodynamics of Fluids*, edited by A. R. GOODWIN, J. SENEGERS, and C. J. PETERS, pp. 215–279, The Royal Society of Chemistry, 2010.
- [86] H. ADIDHARMA and M. RADOSZ, *J. Phys. Chem. B* **105**, 9822 (2001).
- [87] P. FLORY, *J. Am. Chem. Soc.* **58**, 1877 (1936).

- [88] P. FLORY, *J. Am. Chem. Soc.* **74**, 2718 (1952).
- [89] P. FLAJOLET and R. SEDGEWICK, *Analytic Combinatorics*, Cambridge University Press, Cambridge, 1 edition, 2009.
- [90] J. M. TAVARES, P. I. C. TEIXEIRA, M. M. TELO DA GAMA, and F. SCIORTINO, *J. Chem. Phys.* **132**, 234502 (2010).
- [91] H. TORII, *Pure. Appl. Chem.* **76**, 247 (2004).
- [92] N. G. VAN KAMPEN, *Stochastic Processes in Physics and Chemistry*, North-Holland, Amsterdam, 3 edition, 2007.
- [93] M. SCHWARZ and D. POLAND, *J. Chem. Phys.* **63**, 557 (1975).
- [94] P. M. MORSE, *Operations Research* **3**, 255 (1955).
- [95] J. ABATE and W. WHITT, *Queueing Systems* **3**, 321 (1988).
- [96] L. KLEINROCK, *Theory, Volume 1, Queueing Systems*, Wiley-Interscience, 1975.
- [97] A. ALLEN, *Probability, Statistics, and Queueing Theory: With Computer Science Applications*, Computer Science and Scientific Computing Series, Academic Press, cop., 1990.
- [98] G. L. SQUIRES, *Introduction to the Theory of Thermal Neutron Scattering*, Cambridge University Press, Cambridge, 1 edition, 1978.
- [99] D. S. SIVIA, *Elementary scattering theory*, Oxford University Press, Oxford, 1 edition, 2011.
- [100] E. HECHT, *Optics*, Pearson education, Addison-Wesley, 2002.
- [101] S. W. LOVESEY, *Theory of neutron scattering from condensed matter*, Clarendon Press, Oxford, 1 edition, 1984.
- [102] H. FISCHER, A. BARNES, and P. SALMON, *Reports on Progress in Physics* **69**, 233 (2006).
- [103] M. BÉE, *Quasielastic Neutron Scattering, Principles and Applications in Solid State Chemistry, Biology and Materials Science*, Taylor & Francis, 1 edition, 1988.
- [104] F. MEZEI, C. PAPPAS, and T. GUTBERLET, *Neutron Spin Echo Spectroscopy: Basics, Trends and Applications*, Lecture Notes in Physics, Springer, 2003.

- [105] J. J. SAKURAI, *Modern Quantum Mechanics*, Addison-Wesley, Longman, revised edition, 1993.
- [106] D. A. LONG, *The Raman effect: A Unified Treatment of the Theory of Raman Scattering by Molecules*, John Wiley and Sons, Chichester, 1 edition, 2002.
- [107] J. R. SCHMIDT, N. SUNDLASS, and J. L. SKINNER, *Chem. Phys. Lett.* **378**, 559 (2003).
- [108] R. KUBO, *Adv. Chem. Phys.* **15**, 101 (1969).
- [109] J. L. DOOB, *Ann. Math.* **43**, 351 (1942).
- [110] T. PRASANNA, *arXiv:cond-mat/0411553v3*.
- [111] D. FRENKEL and B. SMIT, *Understanding Molecular Simulation, Second Edition: From Algorithms to Applications*, Academic Press, London, 2 edition, 2001.
- [112] N. METROPOLIS, A. W. ROSENBLUTH, M. N. ROSENBLUTH, A. N. TELLER, and E. TELLER, *J. Chem. Phys.* **21**, 1087 (1953).
- [113] W. L. JORGENSEN, D. S. MAXWELL, and J. TIRADORIVES, *J. Am. Chem. Soc.* **118**, 11225 (1996).
- [114] A. K. SOPER, *Empirical Potential Structure Refinement - EPSRshell - A Users Guide*, 2010.
- [115] R. MCGREEVY and L. PUSZTAI, *Mol. Sim.* **1**, 359 (1988).
- [116] R. KONO, T. A. LITOVITZ, and G. E. MCDUFFIE, *J. Chem. Phys.* **45**, 1790 (1966).